Compact Object Modeling in the Globular Cluster 47 Tucanae

Claire S. Ye[1,2] , Kyle Kremer[3,4] , Carl L. Rodriguez[5] , Nicholas Z. Rui[3] , Newlin C. Weatherford[1,2] , Sourav Chatterjee[6] , Giacomo Fragione[1,2] , and Frederic A. Rasio[1,2]

[1] Department of Physics & Astronomy, Northwestern University, Evanston, IL 60208, USA; shiye2015@u.northwestern.edu
[2] Center for Interdisciplinary Exploration & Research in Astrophysics (CIERA), Northwestern University, Evanston, IL 60208, USA
[3] TAPIR, California Institute of Technology, Pasadena, CA 91125, USA
[4] The Observatories of the Carnegie Institution for Science, Pasadena, CA 91101, USA
[5] McWilliams Center for Cosmology and Department of Physics, Carnegie Mellon University, Pittsburgh, PA 15213, USA
[6] Tata Institute of Fundamental Research, Homi Bhabha Road, Mumbai 400005, India

Abstract

The globular cluster 47 Tucanae (47 Tuc) is one of the most massive star clusters in the Milky Way and is exceptionally rich in exotic stellar populations. For several decades it has been a favorite target of observers, and yet it is computationally very challenging to model because of its large number of stars ($N \gtrsim 10^6$) and high density. Here we present detailed and self-consistent 47 Tuc models computed with the `Cluster Monte Carlo` code (`CMC`). The models include all relevant dynamical interactions coupled to stellar and binary evolution, and reproduce various observations, including the surface brightness and velocity dispersion profiles, pulsar accelerations, and numbers of compact objects. We show that the present properties of 47 Tuc are best reproduced by adopting an initial stellar mass function that is both bottom-heavy and top-light relative to standard assumptions (as in, e.g., Kroupa 2001), and an initial Elson profile (Elson et al. 1987) that is overfilling the cluster's tidal radius. We include new prescriptions in `CMC` for the formation of binaries through giant star collisions and tidal captures, and we show that these mechanisms play a crucial role in the formation of neutron star binaries and millisecond pulsars in 47 Tuc; our best-fit model contains ∼50 millisecond pulsars, 70% of which are formed through giant collisions and tidal captures. Our models also suggest that 47 Tuc presently contains up to ∼200 stellar-mass black holes, ∼5 binary black holes, ∼15 low-mass X-ray binaries, and ∼300 cataclysmic variables.

Unified Astronomy Thesaurus concepts: Star clusters (1567); Astronomical simulations (185); N-body simulations (1083); Compact objects (288)

1. Introduction

As laboratories for studying both small-scale stellar physics and gravitational dynamics as well as larger-scale galaxy formation and evolution, globular clusters (GCs) have been a main focus of computational *N*-body modeling for several decades. They are efficient in producing exotic objects such as X-ray binaries (e.g., Clark 1975; Heinke et al. 2005), millisecond pulsars (MSPs; e.g., Ransom 2008), and cataclysmic variables (CVs; e.g., Knigge 2012) given their high stellar densities. GCs may also account for a significant fraction of the overall binary black hole (BH) merger rate in the local universe (Kremer et al. 2020; Rodriguez et al. 2021; Abbott et al. 2021, and references therein). Furthermore, their masses, sizes, and spatial distributions provide unique probes into the formation of their host galaxies (e.g., Choksi et al. 2018).

Among Galactic GCs, 47 Tucanae (47 Tuc) is particularly interesting. It is one of the most dense, massive, and luminous GCs in the Milky Way (Harris 1996, 2010 edition) and contains large numbers of exotic sources, including 28 MSPs (Paulo Freire's pulsar catalog 2021), six low-mass X-ray binaries (LMXBs; Heinke et al. 2005; Miller-Jones et al. 2015), and 43 CVs (Rivera Sandoval et al. 2018) observed to date. Since it is one of the closest GCs to Earth and is located at high Galactic latitude (Harris 1996, 2010 edition), there are plenty of

observational data on 47 Tuc, many of them from the Hubble Space Telescope (HST), Chandra, and more recently also from Gaia. For example, shortly after the launch of HST, Guhathakurta et al. (1992) exploited its ability to resolve individual stars in crowded fields, constructed an accurate color–magnitude diagram (CMD), and placed an upper limit on the mass of compact objects at the cluster center. Subsequent HST campaigns aimed to obtain detailed photometry of the cluster core (de Marchi et al. 1993) and derive stellar luminosity and mass functions (Santiago et al. 1996). CV candidates in the cluster were found through many epochs of observation, long exposure times, and almost continuous observing (Gilliland et al. 1995; Edmonds et al. 1996; Shara et al. 1996). Combining X-ray observations from Chandra and 120 orbits of HST, Edmonds et al. (2003a, 2003b) observed the largest number of optical counterparts to the X-ray sources in any GC, and detected many CVs, active binaries, and constrained the total number of MSPs. More recently, to further explore the dynamical structure of 47 Tuc, several studies obtained proper motions and line-of-sight velocities with HST (e.g., McLaughlin et al. 2006; Watkins et al. 2015; Heyl et al. 2017), Gaia (Baumgardt et al. 2019; Vasiliev & Baumgardt 2021), MUSE (Kamann et al. 2018), and archival/ literature data from a combination of instruments (Baumgardt 2017; Baumgardt & Hilker 2018) to construct velocity distributions and examined the rotation and velocity anisotropy of the cluster (e.g., Bellini et al. 2017).

Extensive previous studies have modeled 47 Tuc using static models, including single-mass King models (e.g., Illingworth & Illingworth 1976), multimass generalizations of King models

(e.g., Da Costa & Freeman 1985), Michie-King models (e.g., Meylan 1988, 1989), models with added rotations (e.g., Davoust 1986; Bellini et al. 2017), and models incorporating the effects of the Galactic tidal field on the structure of the cluster (e.g., Hénault-Brunet et al. 2019). However, there have been few previous attempts at modeling the cluster using the *N*-body method, despite this wealth of observational data on 47 Tuc. This is not surprising since modeling GCs as massive and dense as 47 Tuc requires significant computational time and sophisticated *N*-body codes. It takes more than a year for the current best direct *N*-body code, NBODY6++GPU (Wang et al. 2015), to simulate a massive GC similar to 47 Tuc with ∼10^6 stars. Therefore, the more rapid Monte Carlo technique is necessary to explore the parameter space of initial conditions for 47 Tuc (see Section 2). The only two previous studies of 47 Tuc using *N*-body modeling either rely upon scaling-up of low-mass models (Baumgardt & Hilker 2018), or apply artificially large natal kicks for BHs (Giersz & Heggie 2011) so there were only a few BHs in their models. Models without a realistic number of BHs may still show close matches with observations such as the surface brightness profile (SBP; Giersz & Heggie 2011), but would potentially miss the BH dynamics that also significantly affects other exotic objects through gravitational encounters. To uncover the cluster's dynamical properties and understand all evolutionary pathways that shape the observable properties of 47 Tuc and other similar clusters, we develop accurate and self-consistent models of 47 Tuc that will match different observed cluster features simultaneously. Significantly, these models include most up-to-date prescriptions for compact object formation, which in particular enables us to examine pulsar and BH dynamics in 47 Tuc for the first time.

The CMC Cluster Catalog models in Kremer et al. (2020) are representative of most typical present-day Milky Way GCs, so we first searched for a best-fit 47 Tuc model in the catalog using the χ^2 statistic method (Rui et al. 2021). We found that while some catalog models can match the inner parts of the observed surface brightness and velocity dispersion profiles (VDPs), there are large discrepancies at the outer parts of the good-fit models (see Section 5.1). This illustrates the necessity to simulate custom models for 47 Tuc with smaller core radii (less compact objects, especially BHs) and more low-mass stars to puff up the outer part of the cluster.

This paper is organized as follows. In Section 2, we summarize the main computational methods used to model 47 Tuc, and describe the implementation of tidal capture and collision with giant stars to our cluster simulations. We demonstrate that our 47 Tuc models fit the observations by comparing to multiple observational properties such as the SBP and VDP in Section 3. We show the compact object populations in a best-fit model in Section 4. In Section 5, we discuss models constructed in search of the initial conditions that best agree with the observational data, caveats, and uncertainties in our models. Finally, in Section 6, we summarize our results.

2. Methods

We simulate 47 Tuc using the Cluster Monte Carlo code (CMC; e.g., Rodriguez et al. 2022, and references therein), a public, fully parallelized Monte Carlo code based on classic work by Hénon (1971a, 1971b). It is capable of modeling the complete dynamical evolution of realistic dense star clusters

containing ∼10^6 stars over a Hubble time in just a few days. It allows us to compute self-consistent models of even the largest star clusters, covering the full range of masses all the way to the brightest systems. CMC incorporates all relevant physics, including two-body relaxation, tidal mass loss, and strong dynamical interactions of single stars and binaries (e.g., exchange interactions, tidal capture, direct collisions). Stellar evolution is fully coupled to the stellar dynamics and is computed with the publicly available COSMIC software (Breivik et al. 2020) based on Hurley et al. (2000, 2002). The Fewbody package is used to directly integrate all three- and four-body gravitational encounters (Fregeau et al. 2004; Fregeau & Rasio 2007), including post-Newtonian dynamics for BHs (Antognini et al. 2014; Amaro-Seoane & Chen 2016; Rodriguez et al. 2018a, 2018b). In the following subsections, we describe simulation features adopted here that differ from our past CMC assumptions.

2.1. Tidal Capture

Following the early works of Fabian et al. (1975), Press & Teukolsky (1977), and Lee & Ostriker (1986), we implemented tidal capture of main-sequence (MS) stars into CMC. When a compact object and an MS star or two MS stars fly close during single–single encounters, tidal force will perturb the stars and excite nonradial oscillation within them. The oscillation energy comes from the two objects' kinetic energy, and the stars are captured if the oscillation energy exceeds that of their initial kinetic energy. The amount of energy deposited in a star from one passage of encounter can be written as

$$\Delta E_{\rm osc} = \frac{GM_*^2}{R_*}\left(\frac{M}{M_*}\right)^2 \sum_{l=2}^{\infty}\left(\frac{R_*}{R_p}\right)^{2l+2} T_l(\eta_*), \qquad (1)$$

where M_* and R_* are the mass and the radius of the star, and M is the mass of a compact object or another MS star. R_p is the distance of closest approach. T_l is a dimensionless function measuring energy contribution from different harmonic modes l. η_* is a measure of the duration of periastron passage, and is written as

$$\eta_* = \left(\frac{M_*}{M_* + M}\right)^{1/2}\left(\frac{R_p}{R_*}\right)^{3/2}. \qquad (2)$$

We adopt the fitting formulae obtained from Lee & Ostriker (1986) in Kim & Lee (1999) to calculate the cross sections and pericenter distances R_p. The dimensionless function T_l and the oscillation energy in the MS stars are estimated using the formulae in Portegies Zwart & Meinen (1993), which were calculated by fitting to the hydrodynamical studies (Lee & Ostriker 1986; Ray et al. 1987). We include only the contribution of the quadrupole and octupole terms in the tides, while higher-order corrections do not contribute significantly to the oscillation energy.

Since these prescriptions assumed polytropic stellar models, we apply polytropic index $n = 1.5$ for low-mass MS stars with $M < 0.7\,M_\odot$ and naked helium MS stars, which correspond to star type 0 and 7 in COSMIC (Breivik et al. 2020), respectively. We use $n = 3$ for other MS stars with $M > 0.7\,M_\odot$, corresponding to star type 1 (McMillan et al. 1987; Kim & Lee 1999). For a comparison between the simple polytropic stellar models with detailed stellar models, see Appendix B.

The initial total energy of the two stars at infinity can be written as $E_{\rm orb} = \frac{1}{2}\mu v_\infty^2$, where μ is the reduced mass, and v_∞ is the relative velocity at infinity. We assume that if the total oscillation energy deposited in the stars *during the first passage* is larger than the initial total energy, then the two stars are bound and form a tidally captured binary. The binary semimajor axis immediately after tidal capture is set to be $2R_p$, assuming angular momentum conservation during tidal capture and immediate circularization of the binary after tidal capture. We use this simple treatment of final binary separations to maximize the number of binaries formed from tidal capture (Lee & Ostriker 1986), especially neutron star (NS)–MS star binaries that could become redback MSPs in clusters (see also Section 4.1). In the special cases when Roche lobe overflow starts at $2R_p$, we merge the two interacting objects instead of forming a binary.

2.2. Giant Star Collision

We implemented special treatments for single–single collisions involving giant stars into CMC. Here we define "collision" as when the two interacting objects pass within a small factor of the sum of their radii or the radius of a giant star. When giant star collision is activated in CMC, we assume that a giant star collides with another star or compact object when $R_p \leqslant 1.3R_g$ following Lombardi et al. (2006), where R_p is the pericenter distance between the two objects, and R_g is the radius of the giant star. For the collision of two giants, we set the collision pericenter distance limit to $R_p \leqslant 1.3(R_{g1} + R_{g2})$, where R_{g1} and R_{g2} are the radii of the giants. At the same time, the "sticky-sphere" direct collision prescription ($R_p < R_1 + R_2$, where R_1 and R_2 are the radii) is applied to all other stars, where the mass of the collision product is equal to the total mass of the two colliding objects (Fregeau & Rasio 2007).

These collisions with giant stars can lead to the formation of tight binaries. Qualitatively, we expect a collision involving at least one giant star to proceed similarly to the common-envelope process where the cores orbit inside an extended envelope. Through drag forces, the binary inspirals and deposits energy into the envelope until eventually the envelope is expelled, leaving behind a compact binary. We assume that there is no mass transfer to a companion star from the envelopes of the giant stars during these collisions. For single–single collisions involving only one giant, we assume that a binary star formed consists of the core of the giant star and the interacting MS star or compact object.

To calculate the binary semimajor axis, we adopt Equations (3)–(5) below—Equations (4)–(6) from Ivanova et al. (2006)—based on smoothed particle hydrodynamics simulations (Lombardi et al. 2006). The semimajor axis is chosen as the minimum of $a_{\rm coll}$ and $a_{\rm ce}$ from these equations.

$a_{\rm coll}$ is calculated as

$$a_{\rm coll} = \frac{R_p}{3.3(1 - e_{\rm coll}^2)}, \tag{3}$$

where

$$e_{\rm coll} = 0.88 - \frac{R_p}{3R_g}. \tag{4}$$

$a_{\rm ce}$ can be obtained by solving the equation

$$\frac{(M_g + M)v_\infty^2}{2} + \alpha_{\rm ce}\frac{GM_cM}{2a_{\rm ce}} = \frac{GM_g(M_g - M_c)}{\lambda R_g}, \tag{5}$$

with $e_{\rm ce} = 0$. M_g, M, and M_c are the giant's mass, the mass of the nongiant object, and the core mass of the giant, respectively. $\alpha_{\rm ce} = 1$ and $\lambda = 0.5$ are parameters related to common-envelope evolution (e.g., Hurley et al. 2002; see also discussions in Appendix C).

For collisions between two giant stars, we instead calculate the binary semimajor axis using the expression

$$\begin{aligned}
&\frac{(M_{g1} + M_{g2})v_\infty^2}{2} + \alpha_{\rm ce}\frac{GM_{c1}M_{c2}}{2a_{\rm ce}} \\
&= \frac{GM_{g1}(M_{g1} - M_{c1})}{\lambda R_{g1}} + \frac{GM_{g2}(M_{g2} - M_{c2})}{\lambda R_{g2}}
\end{aligned} \tag{6}$$

where $e_{\rm ce} = 0$. M_{g1}, M_{c1}, M_{g2}, and M_{c2} are the masses and the core masses of the first and second giants, respectively. The final binary is composed of the cores of the two giants, and both giant envelopes are ejected.

In special cases where the MS star or a giant core starts mass transfer after the binary semimajor axis is computed, we assume the collision does not lead to binary formation. Instead we merge the two original interacting objects to avoid Roche Lobe overflow during a common-envelope phase, the outcome of which is highly uncertain. The stellar types of the merger products follow those in Table 2 of Hurley et al. (2002).

2.3. 47 Tuc Simulations

For 47 Tuc simulations, we fix the metallicity $Z = 0.0038$ (Harris 1996, 2010 edition), the Galactocentric distance $r_{\rm gc} = 7.4$ kpc (Harris 2010; Baumgardt et al. 2019), and the initial binary fraction $f_b = 0.022$ (Giersz & Heggie 2011). Binary companion masses are drawn from a flat distribution in mass ratio q, in the range 0.1–1 (e.g., Duquennoy & Mayor 1991). Binary orbital periods are drawn from a distribution flat in log scale from Roche Lobe overflow to the hard/soft boundary, and binary eccentricities are drawn from a thermal distribution (e.g., Heggie 1975). To calculate the tidal radius of a cluster, we assume a circular orbit with radius r_{gc} around the Galactic center and a flat rotation curve of the galaxy with circular velocity $v_{\rm gc} = 220$ km s^{-1}. The tidal radius of a cluster is given by

$$r_t = \left(\frac{GM_{clu}}{2v_{\rm gc}^2}\right)^{\frac{1}{3}} r_{\rm gc}^{\frac{2}{3}}, \tag{7}$$

where M_{clu} is the total mass of the cluster (Spitzer 1987; Chatterjee et al. 2010). This calculation of tidal radius is valid for 47 Tuc since the cluster's orbit in the galaxy has a small eccentricity (<0.2) and is almost circular (Vasiliev & Baumgardt 2021).

Following Giersz & Heggie (2011), we adopt a two-part power-law initial mass function (IMF) with masses in the range of 0.08–150 $M_\odot$, a break mass at 0.8 $M_\odot$, and power-law slopes of $\alpha_1 = 0.4$ and $\alpha_2 = 2.8$ for the lower- and higher-mass parts, respectively. NSs formed from core-collapse supernovae receive natal kicks drawn from a Maxwellian distribution with

Table 1
Initial Conditions for the Best-fit Model

N	γ	r_v	Z	r_{gc}	r_t	M_{min}	M_{br}	M_{max}	α_1	α_2	f_b
3×10^6	2.1	4 pc	0.0038	7.4 kpc	182.17 pc	$0.08\,M_\odot$	$0.8\,M_\odot$	$150\,M_\odot$	0.4	2.8	0.022

Note. From left to right: initial number of stars, Elson profile γ index, initial virial radius, metallicity, Galactocentric distance, initial tidal radius, minimum mass, break mass, and maximum mass in the IMF, respectively, power-law slopes for the lower-mass and higher-mass parts of the IMF, respectively, and initial binary fraction.

a standard velocity deviation $\sigma_{NS} = 265$ km s^{-1} (Hobbs et al. 2005). The natal kicks for NSs from electron-capture supernovae and accretion-induced collapses are also drawn from a Maxwellian distribution but with a smaller standard deviation $\sigma_{ecsn} = 20$ km s^{-1} (Kiel et al. 2008; Ye et al. 2019). We apply mass fallback kicks for BHs and sample their natal kicks from the same Maxwellian distribution for core-collapse NSs but with scaled-down velocities (Fryer et al. 2012). The kicks are reduced in magnitude by a fractional mass of fallback material: $v_{BH} = v_{NS}(1 - f_{fb})$, where v_{NS} is the velocity of an NS drawn from Hobbs et al. (2005) for core-collapse supernovae, and f_{fb} is the fractional parameter of the stellar envelope that falls back upon core collapse (Belczynski et al. 2002; Fryer et al. 2012; Morscher et al. 2015). Compared to Giersz & Heggie (2011), our simulations treat BHs and NSs more realistically by applying fallback BH natal kicks and allowing for NSs to form in electron-capture supernovae and accretion-induced collapses with low kicks, which are essential for explaining the large number of pulsars in GCs (e.g., Pfahl et al. 2002; Podsiadlowski et al. 2004; Ye et al. 2019).

We assume the 47 Tuc models are initially described by Elson density profiles (Elson et al. 1987),

$$\rho(r) = \rho_0 \left(1 + \frac{r^2}{a^2}\right)^{-\frac{\gamma+1}{2}}, \qquad (8)$$

where γ is a free parameter of the power-law slope ($\gamma = 4$ gives a Plummer sphere; Plummer 1911), and a is a scaling parameter.

Unlike previous CMC papers that varied the initial cluster parameter space in a grid format (e.g., Kremer et al. 2020; Weatherford et al. 2021), here we have run 16 simulations (see Table 3 in Appendix D) exploring a specific parameter space for 47 Tuc in the initial number of stars, density profile, binary fraction, virial radius, tidal radius, and IMF to search for a best-fit model where the model cluster's late time (9–13.8 Gyr) SBP and VDP first match the observations. We also vary γ of the Elson profile to analytically fit the outer slope of the observed SBP. All simulations are evolved to 13.8 Gyr. Table 1 shows the initial conditions of our best-fit model for 47 Tuc.

3. Matching Observed Cluster Properties

We found best-fit models by comparing the χ^2 likelihood between different snapshots (time steps) of the simulation and selecting the ones with small χ^2 as in Rui et al. (2021). The model SBP is calculated by making two-dimensional projections at each time step of a simulation, assuming spherical symmetry (also see Kremer et al. 2018b). We exclude very bright stars with luminosity $L > 12\,L_\odot$ to avoid large fluctuations in the SBP, and also low-mass, faint stars with $M \leqslant 0.85\,M_\odot$. Changing the cutoff luminosity from $12\,L_\odot$ to $15\,L_\odot$ has a negligible effect on the SBP fit. We use the method in Pryor & Meylan (1993) to find the model VDP, including in the calculation all giant stars and upper-MS stars with a cutoff

mass $M > 0.85\,M_\odot$ (the MS turn-off mass of the model is ∼0.9 $M_\odot$). Small variations in the cutoff mass for the VDP calculations do not affect the fit. For more details on the SBP and VDP calculations, see Kremer et al. (2018b) and Rui et al. (2021), and the references therein. Similar to the VDP, we use the same selection of stars to calculate the projected model number density profile (NDP). Note that, unlike the VDP, the model NDP is very sensitive to changes in the cutoff mass. The cluster properties only vary negligibly between ∼9 and 12 Gyr, and Figure 1 shows the snapshot at 10.55 Gyr as a representative of the best-fit 47 Tuc models. At this time, the best-fit model is able to closely match the observed SBP, VDP, NDP, and pulsar acceleration distribution simultaneously.

The initial tidal radius of the cluster with a circular orbit at $r_{gc} = 7.4$ kpc is 182 pc. The best-fit cluster starts out to $r_{max} = 800$ pc initially, and is overfilling its tidal radius (r_{max} is a free parameter in our simulations). Observationally, young star clusters (potential GC progenitors) appear to not be tidally truncated, and may be surrounded by unbound stars at the outer region that have not yet been stripped away by the Galactic tidal force (e.g., Elson et al. 1987, 1989; Mackey & Gilmore 2003). Using $r_{max} = 300$ pc only changes the final SBPs, VDPs, and NDPs slightly. Furthermore, it is shown in the top panel of Figure 1 that the model SBP deviates from the observed SBP at the edge of the cluster where $r \gtrsim 1500''$. Attempting to decrease this discrepancy, we tried a simulation with $r_{gc} = 5.5$ kpc (pericenter of the observed 47 Tuc orbit instead of the apocenter at 7.4 kpc; Baumgardt et al. 2019) and initial tidal radius of 149 pc. Although this did lower the outermost portion of the model SBP, the discrepancy was still present. This could be because our models do not take into account rotation (see Section 5.5) or because the observations at the edge of the cluster are incomplete due to contamination from field stars (the fit is better for the NDPs in the bottom panel where the observations at the edge of the cluster are taken with Gaia; de Boer et al. 2019).

The age of 47 Tuc can be estimated by modeling the properties of the cluster's white dwarf (WD) cooling sequence, comparing its CMD to theoretical isochrones, or fitting stellar evolutionary tracks to observed eclipsing binaries in the cluster. The estimated ages are uncertain and span a wide range from ∼9–14 Gyr (e.g., Dotter et al. 2010; Thompson et al. 2010; Hansen et al. 2013; VandenBerg et al. 2013; Brogaard et al. 2017; Thompson et al. 2020, and references therein). Our models predict that the age of 47 Tuc is between ∼9 Gyr to ∼12 Gyr, consistent with these estimates.

Figure 2 compares the best-fit model's velocity anisotropy profile to the observations. Some recent studies (e.g., Vasiliev & Baumgardt 2021) have shown that some GCs exhibit velocity anistropy, which may be caused by rotation. In particular, observations of 47 Tuc (Watkins et al. 2015; Heyl et al. 2017; Vasiliev & Baumgardt 2021) using both HST and Gaia show small velocity anisotropy both in the inner and outer parts of the cluster. Our best-fit model is consistent with being
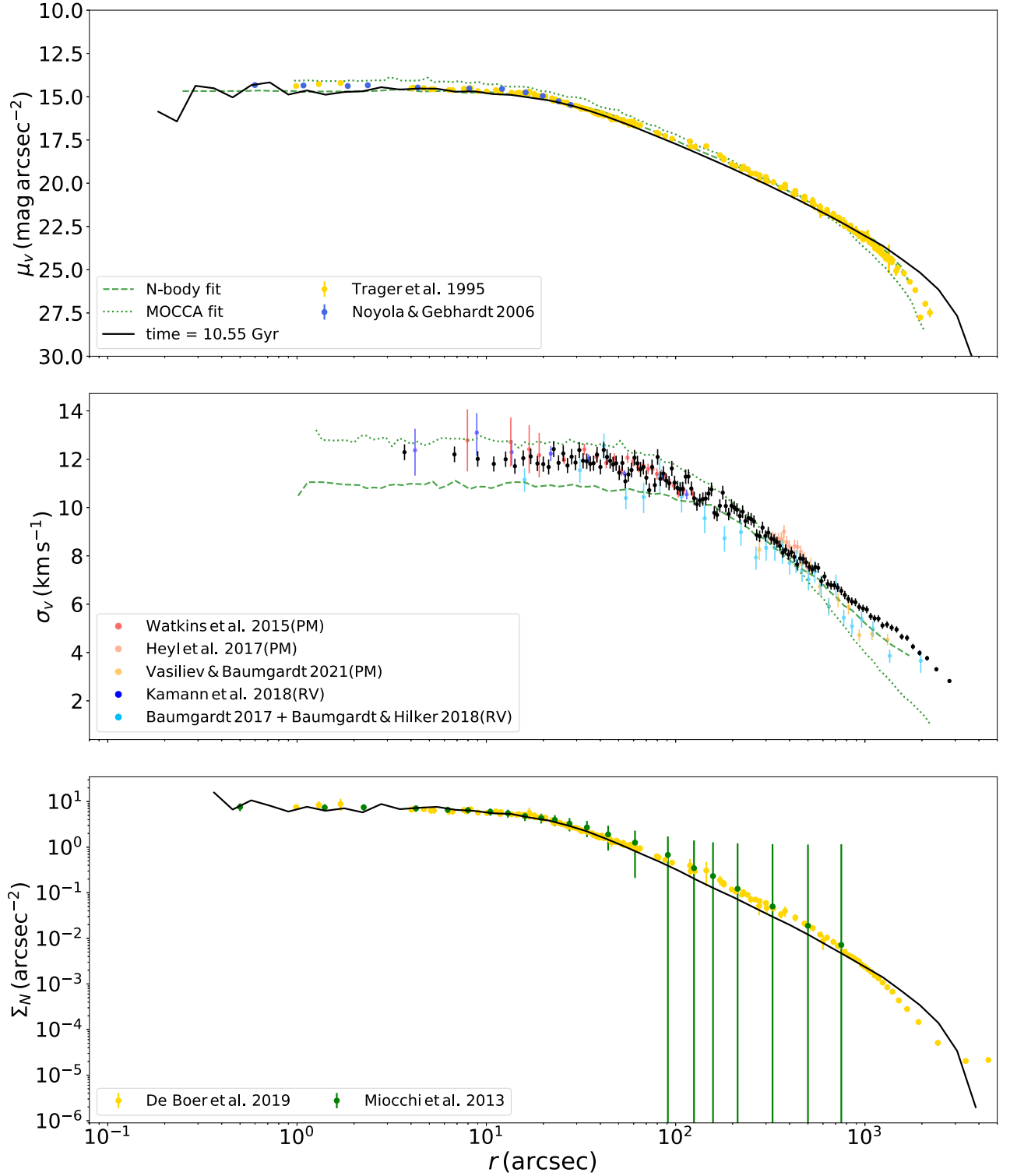
Figure 1. Comparison between our model SBP, VDP, and NDP with the observations. The model profiles are shown by the black curves and black markers. The observed SBPs are from Trager et al. (1995) and Noyola & Gebhardt (2006), VDPs are from Watkins et al. (2015), Heyl et al. (2017), Kamann et al. (2018), Baumgardt (2017), Baumgardt & Hilker (2018), and Vasiliev & Baumgardt (2021), and NDPs are from Miocchi et al. (2013) and de Boer et al. (2019). "PM" stands for proper motion, and "RV" stands for radial velocity. When available, fits from the MOCCA model (dotted curves; Giersz & Heggie 2011) and the direct N-body model (dashed curves; Baumgardt et al. 2021) of 47 Tuc are also shown. Our model profiles agree well with the observations.

isotropic and, overall, is within the velocity anisotropy uncertainties of the observations.

Since 47 Tuc contains the second largest population of MSPs (28 observed to date; Paulo Freire's pulsar catalog 2021), 47 Tuc models must be able to explain its pulsar accelerations in the cluster potential. Accurate pulsar line-of-sight accelerations are obtainable from timing analysis of pulsar binary orbital periods. Upper limits on the acceleration are also calculable from the pulsar spin derivatives, in the case of an isolated pulsar or binary with incomplete timing (Ridolfi et al. 2016; Freire et al. 2017;
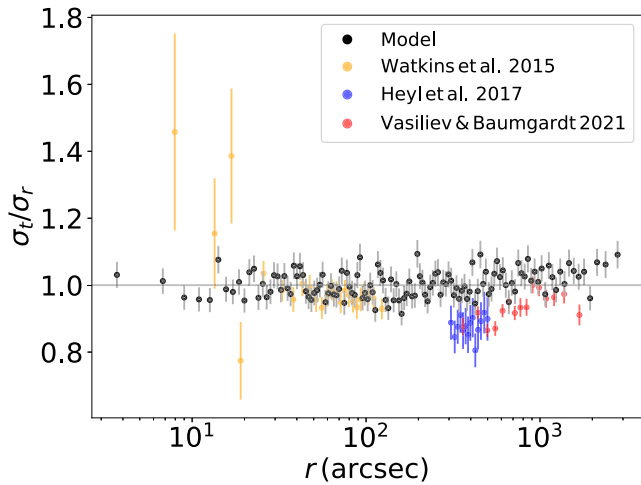
Figure 2. Ratio between the tangential and the radial velocity dispersions. Similar to Figure 1, black markers show the best-fit model. Observations (Watkins et al. 2015; Heyl et al. 2017; Vasiliev & Baumgardt 2021) show slight tangential velocity anisotropy in the inner part and radial velocity anisotropy in the outer part. The model is isotropic in general but still within the uncertainties of the observational points.

Freire & Ridolfi 2018; Ridolfi et al. 2021). The observed line-of-sight accelerations and upper limits for 47 Tuc MSPs are shown in Figure 3 (left panel, orange and black markers[7]).

We estimate the maximum line-of-sight accelerations of model pulsars using Equation (2.5) in Phinney (1992),

$$\max|a_l| \approx 1.1 \frac{GM_{\mathrm{cyl}}(<R_\perp)}{\pi R_\perp^2}, \qquad (9)$$

where M_{cyl} is the mass of the cluster within a cylindrical tube of projected radius $R_\perp$ from the cluster center along the line of sight. This is shown by the green curves in Figure 3 (left panel). We also include the distribution of maximum possible acceleration allowed by the cluster potential in Figure 3 (left panel, blue curves), calculated by $\frac{GM(<r)}{r^2}$, where M is the mass within a sphere of radius r. To 1σ uncertainty, all but one of the observed pulsars have line-of-sight accelerations within the bounds allowed by the model potential, demonstrating further that our best-fit model is consistent with the observations. The only outlier at $\sim 4''$ is still enclosed by the maximum possible *total* acceleration allowed by the cluster potential.

The right panel of Figure 3 shows the cumulative number of all model NSs (light blue curve), model MSPs (orange curve), and observed 47 Tuc MSPs (black curve) as a function of the projected distance from the cluster center. All of the observed 47 Tuc pulsars are MSPs with spin periods <30 ms. As expected, the observed MSP distribution agrees better with the modeled MSP distribution than the total NS distribution. The total NS population is distributed slightly farther out because MSPs are formed through extended periods of mass accretion and are slightly more massive ($\sim 0.1\,M_\odot$ more) than most other

NSs. Mass segregation leaves the MSPs closer to the cluster center than typical NSs. Also, NSs closer to the cluster center are more dynamically active, so they more easily acquire companion stars through encounters and become MSPs (Ye et al. 2019).

Table 2 lists the properties of the best-fit 47 Tuc models at the present day, including the total numbers of compact objects and blue straggler stars (BSSs). In addition, Table 4 in Appendix D shows the more general mean and standard deviation values of the same properties for best- and near-fit models from simulations 1–3 in Table 3. The inclusion of simulation 3 with a high initial binary fraction leads to large standard deviations for the numbers of some compact objects. Figure 4 shows the cumulative number distributions of all stellar populations (colors denoted in legend) at an early and a late time of the 47 Tuc simulation. As expected, the cluster core is dominated by BHs due to mass segregation, mixing with the most numerous MS stars initially (see also Kremer et al. 2020), and also WDs at late times. This is also reflected in the cluster's SBP, where it is flat within $\sim 20''$, consistent with the features of a non-core-collapsed cluster.

4. Exotic Objects in 47 Tuc

Here we report the number of exotic objects in the best-fit 47 Tuc model, which can be used to estimate the total numbers of compact objects, including BHs, MSPs, LMXBs, CVs, and numbers of BSSs, in 47 Tuc. Most compact object binaries discussed below, including the binary BHs in Section 5.3, are formed through dynamical interactions; only $\sim 10\%$ of MSPs and $\sim 35\%$ of CVs are formed in primordial binaries. This high fraction of dynamical compact object binaries is not surprising given the high density of the 47 Tuc models and the low initial primordial binary fraction we adopted, which is motivated by observations of 47 Tuc (Milone et al. 2012; see also Section 5.4).

4.1. Pulsars

A total of 28 pulsars (all of them MSPs) have been observed in 47 Tuc, and 18 of them are in binaries (Paulo Freire's pulsar catalog 2021). Among the MSPs in binaries, six of them are "black widow" MSPs with low-mass, planet- or white/brown dwarf-like stellar remnant companions ($\lesssim 0.05\,M_\odot$), and three are "redback" MSPs with MS star-like, nondegenerate companions (~ 0.1–$1\,M_\odot$; Roberts 2013; Kaplan et al. 2018; Strader et al. 2019; Paulo Freire's pulsar catalog 2021, figures and references therein). Both black widows and redbacks have tight orbital periods of $\lesssim 1$ day.

On average between ~ 9–12 Gyr, there are a total of ~ 49 MSPs per snapshot, ~ 23 in binaries, and ~ 26 isolated.[8] Specifically at 10.5 Gyr, there are 26 isolated MSPs, 22 binary MSPs, and 0 young pulsars (spin period >30 ms). Most of the MSPs (32 of them) are formed through collisions with giant stars. Most of these giant star collisions occur between a giant star and an MS star, where the giant star's core becomes an NS in subsequent binary and stellar evolution (see also Section 2.2). A few of the giant star collisions are between a

---

[7] We adopt the accelerations and their uncertainties for MSPs in binaries from the original timing analysis, which used a slightly different 47 Tuc distance (4.69 kpc in Freire et al. 2017) than that used in this paper (4.52 kpc; Baumgardt & Vasiliev 2021) since the distance change has a negligible effect on the accelerations (second term on the right side of Equation (13) in Freire et al. 2017). We have updated the upper limits for MSPs without orbital period timing using the latest 47 Tuc distance measurement from Gaia (Baumgardt & Vasiliev 2021).

[8] We count the 26 MSPs with very low-mass ($\lesssim 0.01\,M_\odot$) CO/ONeMg WD companions, where the WDs are likely unstable as isolated MSPs. This is because there may exist minimum masses for WDs with sufficiently high temperatures ($T \gtrsim 10^4$K) during mass transfer, where there is no equilibrium solution of the WDs' equation of states and the WDs may "evaporate" (Bildsten 2002; Deloye & Bildsten 2003).
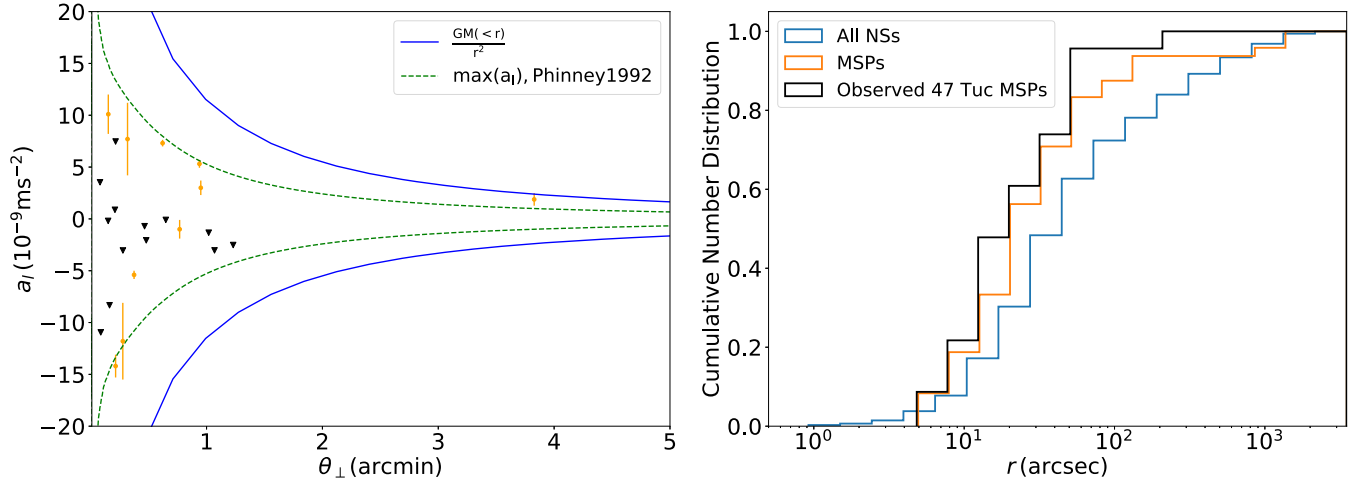
Figure 3. Left: observed pulsar line-of-sight accelerations as a function of angular offsets from the cluster center (orange and black markers; Ridolfi et al. 2016; Freire et al. 2017; Freire & Ridolfi 2018; Ridolfi et al. 2021). The black inverted triangles show the acceleration upper limits of isolated pulsars or pulsars in binaries without orbital period data. The orange markers show the accelerations and their uncertainties for pulsar binaries with orbital period timing. The blue solid curves show the maximum possible accelerations from the model cluster potential, and the green dashed curves show the maximum model line-of-sight accelerations. Right: cumulative number distribution of NSs and MSPs as a function of projected distances from the cluster center. The black curve is the observed pulsar distribution, the orange curve is the model MSP distribution, and the light blue curve is the model distribution for all NSs.

Table 2
Present-day Properties of the Best-fit Models

	μ	σ	Obs.	Reference
Mass($M_\odot$)	1.01×10^6	1.28×10^4	...	...
r_c(pc)	0.89	0.03	...	...
r_h(pc)	6.56	0.15	...	...
r_{cobs}(arcmin)	0.35	0.02	0.36	(1)
r_{hlobs}(arcmin)	2.71	0.14	3.17	(1)
N_{BH}	186	14	1	(3)
N_{BH-BH}	3	1	...	...
N_{NS}	1368	1	...	...
N_{LMXB}	14	2	6	(2)(3)(4)
N_{MSP}	54	3	28	(5)
$N_{young\ psr}$	0	0	0	(5)
N_{CV}	260(334)	19(21)	43 − 370	(4)(6)
N_{BSS}	100(101)	4(5)	114	(7)

Note. From top to bottom: total mass, theoretical core radius, theoretical half-mass radius, observational core radius, observational half-light radius, number of BHs, number of binary BHs, number of NSs, number of LMXBs, number of MSPs (including tidally captured NS–MS binaries), number of young pulsars (spin period >30 ms), number of CVs within theoretical half-mass radius (total number in the model), and number of BSSs within theoretical half-mass radius (total number in the model). The mean values μ are averages over 3 Gyr from ∼9 Gyr to ∼12 Gyr calculated using at least 19 snapshots, and σ are the standard deviations. (1) Harris (1996, 2010 edition), (2) Heinke et al. (2005), (3) Miller-Jones et al. (2015), (4) Bhattacharya et al. (2017), (5) Paulo Freire's pulsar catalog (2021), (6) Rivera Sandoval et al. (2018), and (7) Parada et al. (2016). The theoretical core radius is mass-density-weighted and calculated using the method in Casertano & Hut (1985). The model observational half-light radius is defined to be the two-dimensional-projected radius that contains half of the cluster's total light, and the model observational core radius is estimated using the method described in Morscher et al. (2015) and Chatterjee et al. (2017).

WD and a giant star. Figure 5 shows the distribution of formation times of all MSPs formed in a Hubble time in the best-fit 47 Tuc simulation. At early times of the cluster's evolution ($\lesssim 3$ Gyr), collisions with giant stars play a significant role (∼80%) in forming the binaries that host MSPs later, or lead to more binary-mediated dynamical encounters and subsequent MSP formation. This is shown by the peak in the formation time distribution in Figure 5. After ∼3 Gyr, more than half of the BHs have been ejected and the cluster is denser than earlier. The higher density leads to enhanced dynamical interactions and the formation of subsequent MSP-host binaries through exchange encounters or tidal capture. In total, ∼40% of MSPs formed after 3 Gyr.

In Figure 6, we further compare the orbital periods and companion masses of *all* model MSP binaries and tidally captured NS–MS star binaries from 9–12 Gyr to the observations. Roughly speaking, CMC models can produce all three groups of pulsar binaries that bracket the ones observed (black widows, redbacks, and MSPs with WD companions, respectively). It is important to point out that tidal capture can produce redback-like NS–MS star binaries (orange circles in Figure 6, five per snapshot) with similar companion masses and orbital periods, but these five NSs are not spun up to MSPs in the models. In a realistic scenario during tidal capture, an MS star is likely to expand from the injection of orbital energy and fill its Roche Lobe (e.g., Kochanek 1992). Thus it is reasonable to assume that a captured, puffed-up MS star can transfer mass to an NS and spin it up to an MSP. However, CMC currently lacks detailed treatments of MS stars in tidal capture interactions, and COSMIC does not include the latest pulsar physics such as pulsar irradiation (e.g., Chen et al. 2013; Ginzburg & Quataert 2020, and references therein). We will consider these details and study model MSPs and tidal-captured NS–MS star binaries that overlap with the observed pulsar binaries in future works.

In total, the best-fit model produced 54 MSPs including the NS–MS star binaries formed in tidal capture interactions. This number is larger than the actual observed number of MSPs in 47 Tuc likely because pulsar searches are limited by selection effects such as the interstellar dispersion and scattering, and survey thresholds (e.g., Lorimer 2008, and references therein). Our estimate is consistent with the upper-limit estimates of the potential total number of MSPs in 47 Tuc from previous studies (Heinke et al. 2005; Abdo et al. 2009).
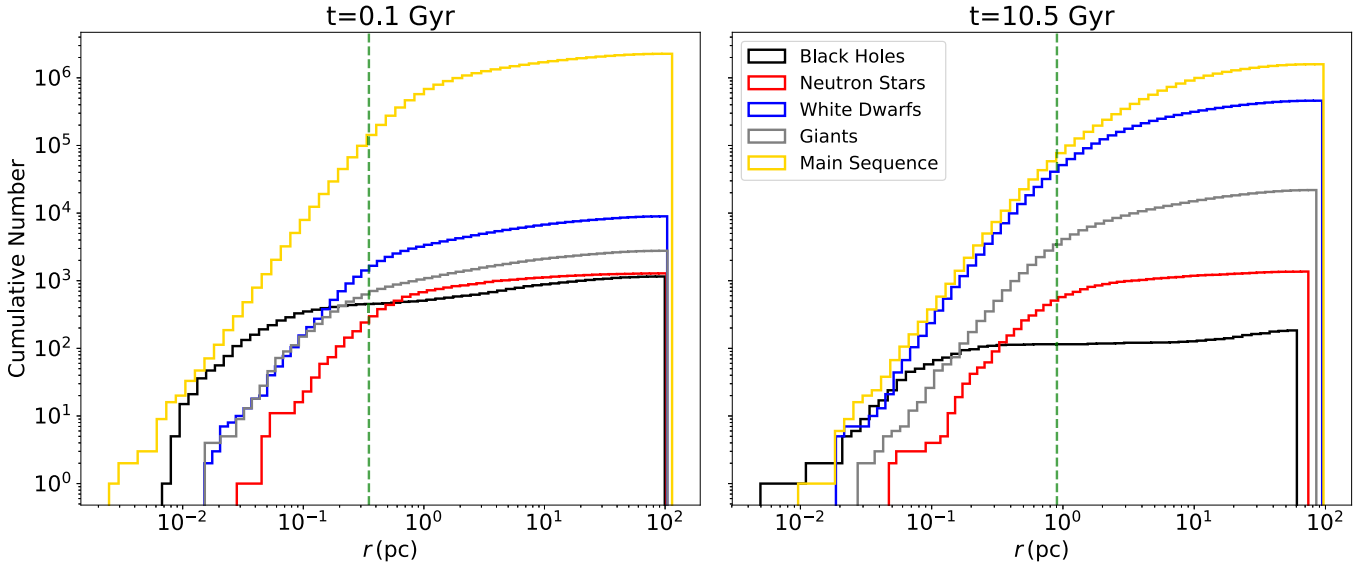
Figure 4. Cumulative number distributions of all stellar populations at 0.1 Gyr (left panel) and at 10.5 Gyr (right panel) as the function of their distances to the cluster center in three dimensions. The vertical dashed lines show the theoretical core radii.
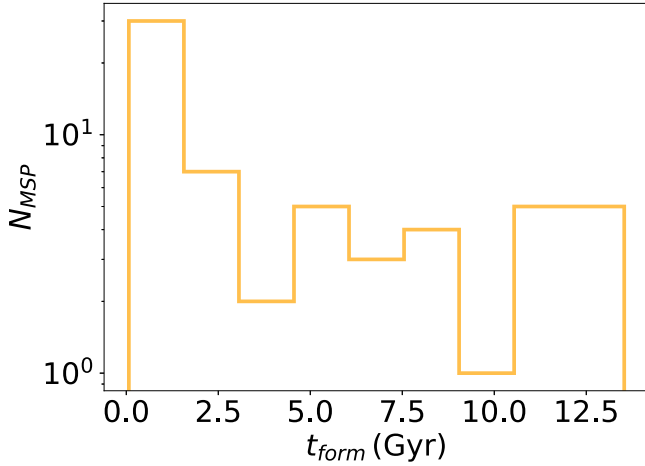

Figure 5. Formation time distribution of all MSPs ever formed in the best-fit 47 Tuc simulation in a Hubble time.

Figure 6. Orbital periods vs. companion masses of MSP binaries in 47 Tuc. The stars show the observed 47 Tuc MSPs. Black stars are black widows, red stars are redbacks, and blue stars are "normal" MSPs with WD companions. Model MSPs are shown by green triangles, and NS–MS star binaries from tidal capture are shown by orange circles.

4.2. Low-mass X-Ray Binaries and Cataclysmic Variables

Observations have detected 370 X-ray sources within $2'.79$ of 47 Tuc using the Chandra Observatory (Heinke et al. 2005; Bhattacharya et al. 2017) and found ∼5 quiescent LMXBs (Heinke et al. 2005). Later studies have further confirmed 43 CVs (Rivera Sandoval et al. 2018) and found one candidate BH LMXB (Miller-Jones et al. 2015; Bahramian et al. 2017).

We define LMXBs as BHs or NSs in mass-transferring binaries with WD, giant star, or MS star companions in our models. There are ∼14 LMXBs on average per snapshot on the timescale of 3 Gyr in our best-fit models, where ∼3 are NS–MS star binaries, ∼5 are BH-WD binaries, ∼1 is a BH–giant star binary, and ∼5 are BH–MS star binaries. There are a similar number of LMXBs at 10.5 Gyr. Similar to LMXBs, we define CVs as mass-transferring WD binaries with MS star companions (e.g., Kremer et al. 2021). There are on average ∼334 CVs at ∼9–12 Gyr, and a similar number at 10.5 Gyr. Most of the CVs (∼260) and almost all of the LMXBs identified in our models are within the theoretical half-mass radius, consistent

with the detected number of X-ray sources. These are only general comparisons between the number of LMXBs and CVs in models and from observations, since we do not consider properties such as duty cycles and luminosities of these mass-transferring binaries. It is not surprising that our models predict more LMXBs and CVs than are observed. The observations of LMXBs and CVs are also limited by selection effects, including the stellar crowdedness in GCs and the faintness of some of these binary systems (Heinke et al. 2003 estimated that there are seven times more quiescent LMXBs than bright LMXBs in GCs). The number of CVs from the best-fit 47 Tuc models is consistent with the estimates in Ivanova et al. (2006) and Rivera Sandoval et al. (2018), which showed that clusters similar in mass to 47 Tuc can have ∼300 CVs. This provides more support for the number estimates of compact objects in our 47 Tuc models.
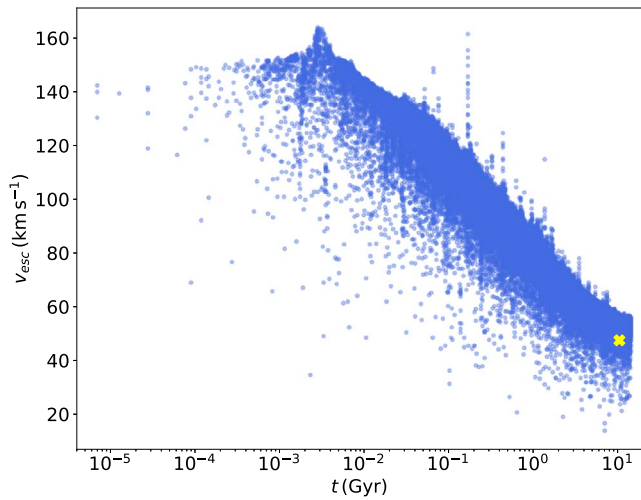
Figure 7. Escape velocities during strong interactions (single–single, binary–single, and binary–binary encounters) as a function of time. The escape velocities of the cluster decrease about three times from ∼160 to ∼60 km s⁻¹ over a Hubble time. The yellow cross marker shows the central escape velocity (47.5 km s⁻¹) of 47 Tuc from Holger Baumgardt's catalog (https://people.smp.uq.edu.au/HolgerBaumgardt/globular/parameter.html), assuming 10.5 Gyr.

4.3. Black Holes

47 Tuc has one observed BH X-ray binary candidate (47 Tuc X9; Miller-Jones et al. 2015; Bahramian et al. 2017). Recently, Weatherford et al. (2020) used mass segregation measurements to infer a total population of 43^{+146}_{-37} (2σ uncertainties) stellar-mass BHs in 47 Tuc, a few percent of which may be found in mass-transferring binaries similar to the X9 source (e.g., Kremer et al. 2018a). It has also been suggested that 47 Tuc may host an intermediate-mass BH (Kızıltan et al. 2017) with a mass of $2300^{+1500}_{-850}\,M_\odot$.

Initially, the model cluster produced ∼1270 BHs. Most of them are ejected later through dynamical interactions, as the escape velocities of the cluster decrease significantly over a Hubble time (Figure 7). On average there are ∼186 BHs and ∼3 binary BHs over a 3 Gyr timescale from ∼9 Gyr to ∼12 Gyr, while there are 182 BHs and two binary BHs at the best-fit model. The number of retained BHs at present is consistent with the 2σ upper limit, and the total mass of the BHs per snapshot (∼2350 $M_\odot$) is consistent with the 1σ upper limit in Weatherford et al. (2020). However, the BH mass in our best-fit models is twice as large as in Hénault-Brunet et al. (2019), indicating different IMFs may vary the final retained BH mass significantly (although they did not specify the maximum and minimum masses used in their IMF). Furthermore, the total mass of BHs in the 47 Tuc models is about the same as the mass of a potential intermediate-mass BH in the cluster (Kızıltan et al. 2017). However, since the pulsar accelerations in 47 Tuc can be reproduced with a group of stellar-mass BHs, the existence of an intermediate-mass BH is not necessary (also see Mann et al. 2019). We will study how an intermediate-mass BH affects the properties of a cluster in future works.

4.4. Blue Stragglers

We define model BSSs based on the MS star turn-off (TO) luminosity, where the model MS stars reach the highest
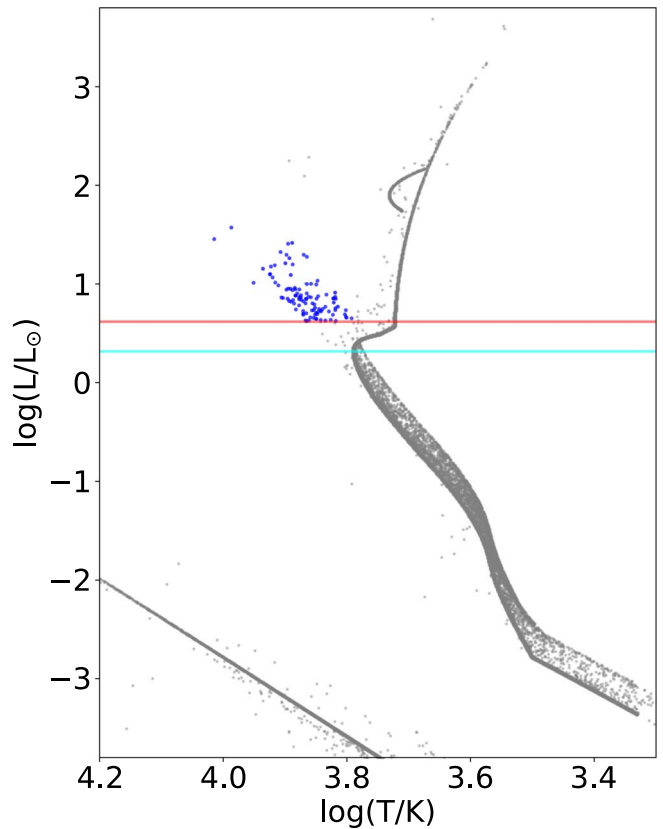

Figure 8. H-R diagram of the best-fit model. Blue dots show the BSSs. There are 108 BSSs at this time. The aqua line shows the turn-off luminosity L_{TO} of the MS stars, and the red line is at twice the turn-off luminosity. The BSSs are selected from upper-MS stars with $L > 2L_{TO}$ and $T > T_{TO}$.

temperature. Temperatures of isolated stars are calculated using the stars' luminosities and radii (COSMIC outputs) assuming a blackbody radiation model, and temperatures of binary stars are calculated from the combined luminosity-weighted temperature of the component stars, where the total luminosity of a binary is the sum of the luminosities of its component stars (Weatherford et al. 2018, Equation (1)). To avoid contamination from normal MS stars, we specify BSSs as upper-MS stars with temperature $T > T_{TO}$ and luminosity $L > 2L_{TO}$, either isolated or in binaries (e.g., Kremer et al. 2020).

Parada et al. (2016) detected 114 BSSs using UV data taken from HST of 47 Tuc at ≲160″. In our models, we find a total of ∼101 BSSs per unit time, and ∼100 of them are within the theoretical half-mass radius (see Figure 8 and Table 2), less than the observed number of BSSs. This may be because COSMIC under-produces BSSs through the mass transfer channel (Leiner & Geller 2021). Most BSSs (≳95%) in the 47 Tuc models are formed in direct collisions of MS stars. In addition, the 2σ upper limit of the number of BSSs (Table 2) is very close to the observed number of BSSs, suggesting that the potential under-production of BSSs through the mass transfer channel is only a small effect in 47 Tuc.

The lifetime of BSSs in the best-fit model is also shown in Figure 9 (upper panel). All of them have lifetimes ≲2 Gyr. With the short lifetimes and the continuing formation of BSSs through stellar collisions, the average number of BSSs at late times of the cluster's evolution (Figure 9; bottom panel) is quite stable.
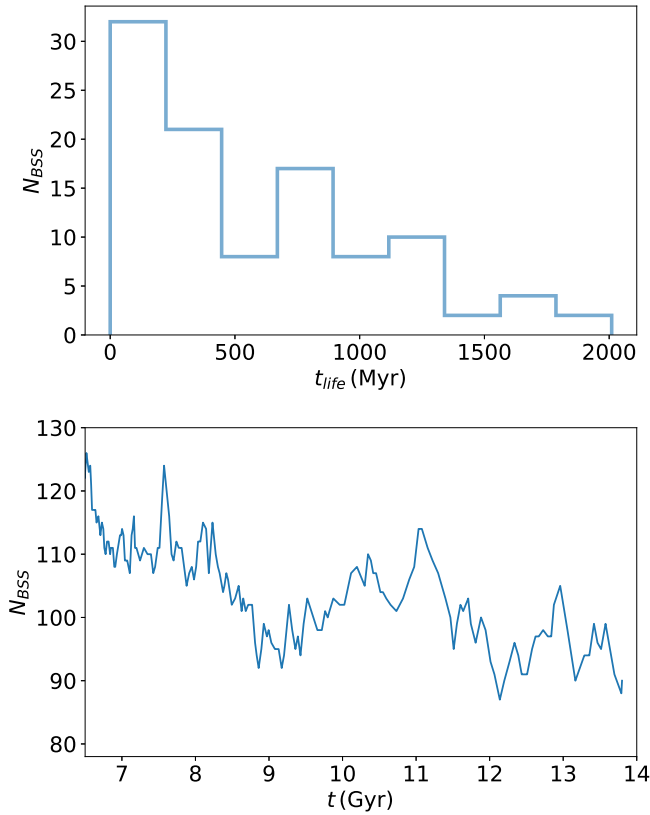
Figure 9. Top panel: lifetime distribution of BSSs in the best-fit model as shown in Figure 8. All of the BSSs have a lifetime $\lesssim 2$ Gyr. Bottom panel: number of BSSs as a function of time at late times of the cluster's evolution.

Figure 10. Top 10 closest-fit models for 47 Tuc (gray curves) from the CMC Cluster Catalog (Kremer et al. 2020). Nine of them are different time steps from the same simulation, where initially it has a canonical mass function from Kroupa (2001), number of stars $N = 1.6 \times 10^6$, King concentration parameter $W_0 = 5$, virial radius $r_v = 1$ pc, and binary fraction $f_b = 5\%$. The metallicity is $Z = 0.002$ and the Galacticocentric distance is 8 kpc. The last model is from a simulation with initial $r_v = 2$ pc, and the other initial conditions are the same as in the above simulation.

5. Discussion

5.1. King Profile versus Elson Profile

Many previous studies have shown that a King profile (King 1966) may not be the best match for the observed SBPs of the majority of GCs in the Milky Way because of its sharp cutoff of the density distribution close to the tidal radius (e.g., McLaughlin & van der Marel 2005; Miocchi et al. 2013; de Boer et al. 2019; Hénault-Brunet et al. 2019). Instead, the Wilson profile (Wilson 1975), which is more spatially extended than the King profile, is shown to fit equally well or better where the observed SBPs exhibit a smoother decrease in the outermost radial density (e.g., McLaughlin & van der Marel 2005; Miocchi et al. 2013; de Boer et al. 2019). More recently, studies have demonstrated that multimass models from the LIMEPY family (Gieles & Zocchi 2015) represent some GCs better than the King or the Wilson profile, including 47 Tuc (de Boer et al. 2019; Hénault-Brunet et al. 2019). LIMEPY models are isothermal in the central regions and are described by polytropes in the outer regions. They can reproduce King or Wilson profiles with certain choices of truncation parameter. Furthermore, it has been shown that young star clusters in the Large Magellanic Cloud are better described by an Elson profile with no apparent tidal truncation (Elson et al. 1987; Mackey & Gilmore 2003). The Elson profile is a generalization of the Plummer profile (Plummer 1911) that arises when $\gamma = 4$ in Equation (8). The Elson profile is similar to the King profile in the inner regions of a cluster, but exhibits larger density or surface brightness at radii approaching the tidal radius (see Figure 4 in Mackey & Gilmore 2003). A
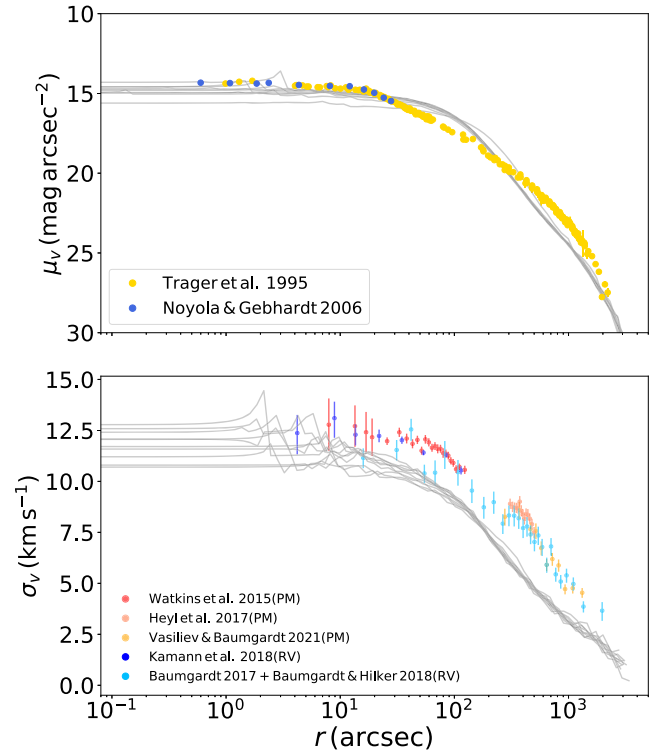
typical range of γ for young star clusters in the Large Magellanic Cloud is ~ 2.2–3.2 (Mackey & Gilmore 2003; Portegies Zwart et al. 2010), close to what we adopt for 47 Tuc.

Figure 11 shows how 47 Tuc's observed SBP and VDP are fit by a massive model with a King profile (as opposed to the best-fit model using an Elson profile shown in Figure 1). The top panels of Figures 1 and 11 show that models using both profiles can fit the observed SBP. However, the King profile model starts to deviate from observations at around $300''$, which encloses $\sim 20\%$ of the model's total mass. We also explored whether varying the tidal radius of the King models could improve their fit to the outer part of the SBP. Changing the Galactocentric distance from 47 Tuc's apocenter 7.4 kpc to its pericenter 5.5 kpc (Baumgardt et al. 2019), thereby shrinking the tidal radius of the cluster, does not affect the SBP. This indicates that models with a King profile are underfilling. Furthermore, we also ran a set of small models (initial masses $\sim 2 \times 10^5 M_\odot$) with different initial King concentration parameters $W_0 = 3$, 5, 7, and 9 in order to alter the cluster potential's shape. We find that unless W_0 is very large ($\gg 9$), there is no apparent change in the final SBPs. More importantly, the model VDP does not match the observed VDP of 47 Tuc (Figure 11, bottom panel). Figure 10 further demonstrates that a flatter density profile than the King profile is needed to explain the observed VDP at radii $\gtrsim 50''$. Taking all of these into account, we adopt the Elson profile for better fits to the outer part of the cluster in this study.
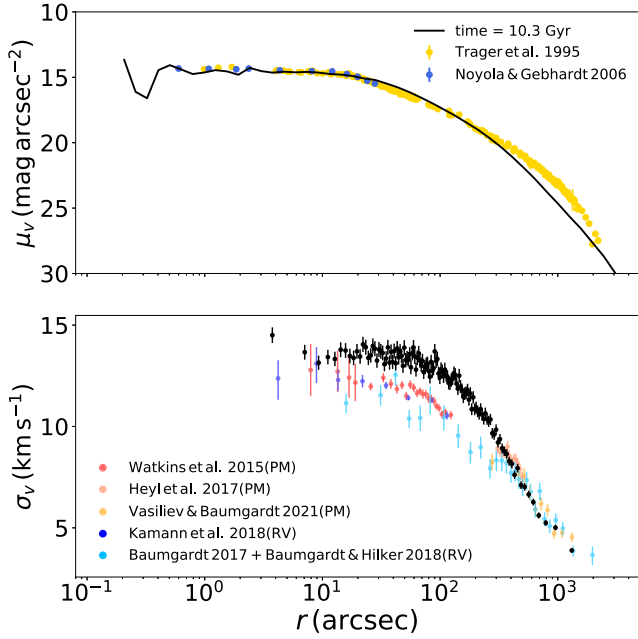
Figure 11. A massive CMC model with a King profile (the black curve and black markers). This model has an initial number of stars $N = 2 \times 10^6$, initial King concentration parameter $W_0 = 7.5$, and an initial virial radius $r_v = 1.4$ pc. Its initial binary fraction, IMF, metallicity and Galactocentric distance are the same as the best-fit 47 Tuc models (Table 1). These initial conditions are chosen such that the model SBP can match the observed 47 Tuc SBP.

5.2. Initial Mass Function

Whether or not the IMF is universal for GCs is still an ongoing debate. For example, Marks et al. (2012) found that stellar IMFs are more top-heavy (more high-mass stars) as a cluster's metallicity becomes lower and the gas density of the pre-GC cloud becomes larger. Later, Haghi et al. (2017) showed that top-heavy IMFs can better explain the relation between the observed mass-to-light ratios and the metallicities of GCs in the Andromeda galaxy. However, in contrast to the suggested initial power-law slope for the mass function of massive stars ($\gtrsim 1\,M_\odot$) in 47 Tuc (Marks et al. 2012), both Giersz & Heggie (2011) and Hénault-Brunet et al. (2019) found that steeper power-law slopes (comparing to Kroupa 2001) better match the 47 Tuc observations. The power-law slope we adopt for high-mass stars ($\alpha_2 = 2.8$ for $0.8 \leqslant m/M_\odot$ in Table 1) is roughly within the 95% uncertainties of the Kroupa IMF ($\alpha_2 = 2.3 \pm 0.3$ for $0.5 \leqslant m/M_\odot < 1.0$ and $\alpha_3 = 2.3 \pm 0.7$ for $1 \leqslant m/M_\odot$; Kroupa 2001) except that we use a different break mass. This indicates that 47 Tuc may be top-light.

We also ran simulations with $\alpha_2 = 2.3$, 1.8 (the initial mass and other initial conditions are the same as in Table 1) to further check if a power-law slope for massive stars more consistent with the Kroupa IMF or a top-heavy IMF is allowed. Figure 12 shows the SBP and VDP of a model at 10.55 Gyr with an initial $\alpha_2 = 2.3$. Because the shallower IMF increases the number of massive stars and BHs, the model is puffier (having larger core radius from BH burning; e.g., Kremer et al. 2019) and does not fit either the observed SBP or VDP. The simulation with initial $\alpha_2 = 1.8$ dissolved before 5 Gyr due to even more extreme BH burning (e.g., Chatterjee et al. 2010; Weatherford et al. 2021).

It is significant to point out that a top-light IMF may not be the only way to produce a good fit for 47 Tuc. There may be a degeneracy between having a top-light IMF or instead, having
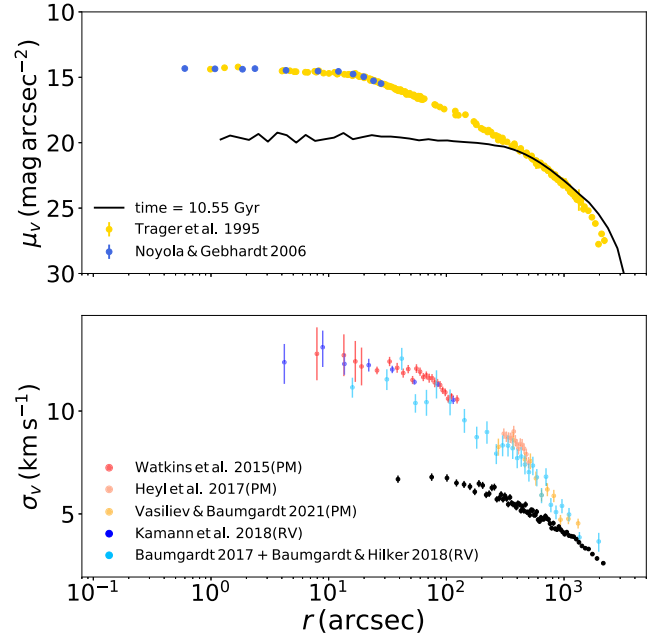

Figure 12. A massive model at $t = 10.55$ Gyr with initial $\alpha_2 = 2.3$ and initial $N = 1.96e6$ (the black curve and black markers). The initial N is lowered to keep the initial mass of this model the same as that of the best-fit model. All other initial conditions are the same as the best-fit model.

a smaller initial virial radius r_v; both can reduce the number of BHs and the cluster core radius. A smaller initial r_v corresponds to a shorter two-body relaxation time (Spitzer 1987) and a faster dynamical clock for the cluster (Kremer et al. 2019). Thus a model with smaller r_v will process and eject its BHs faster through dynamical encounters in the same time (e.g., 13 Gyr). However, for 47 Tuc and similar simulations with large initial masses ($\sim 2.5 \times 10^6\,M_\odot$), a simulation with a smaller initial r_v of $\lesssim 1$ pc takes a much longer time than simulations with $r_v > 1$ pc (>2 months compared to 2 weeks). Therefore we do not explore small r_v models in this paper, and leave them for future studies (e.g., N. C. Weatherford et al. 2022, in preparation).

Furthermore, Hénault-Brunet et al. (2019) found that a power law with $\alpha_1 = 0.52$ for $m/M_\odot < 0.5$ and $\alpha_2 = 1.35$ for $0.5 < m/M_\odot < 1$ for their 47 Tuc models matched the observations. This together with the IMF used for 47 Tuc modeling in Giersz & Heggie (2011), which we also adopted here, all have shallower power-law slopes for lower-mass stars than the Kroupa IMF ($\alpha_1 = 1.3 \pm 0.5$ for $0.08 \leqslant m/M_\odot < 0.5$ and $\alpha_2 = 2.3 \pm 0.3$ for $0.5 \leqslant m/M_\odot < 1$; Kroupa 2001). In addition, Baumgardt & Hilker (2018) derived a global power-law slope of 0.53 for $0.2 < m/M_\odot < 0.8$ for 47 Tuc. This is slightly steeper than the 0.4 present-day mass function slope for $\sim 0.2 < m/M_\odot < 0.7$ in our 47 Tuc model, which could be due to the selection bias against faint low-mass stars in the crowded central area of 47 Tuc. In Section 3 we show that, by adopting an IMF that is both bottom-heavy and top-light, we can produce models that match the 47 Tuc observations. However, we have only explored a small set of initial parameters and did not vary the lower-mass power-law slope of the IMF because the 47 Tuc-size simulations are very computationally expensive. It is possible a power-law slope for lower-mass stars that are more consistent with those in the Kroupa IMF may be able to produce a 47 Tuc model.
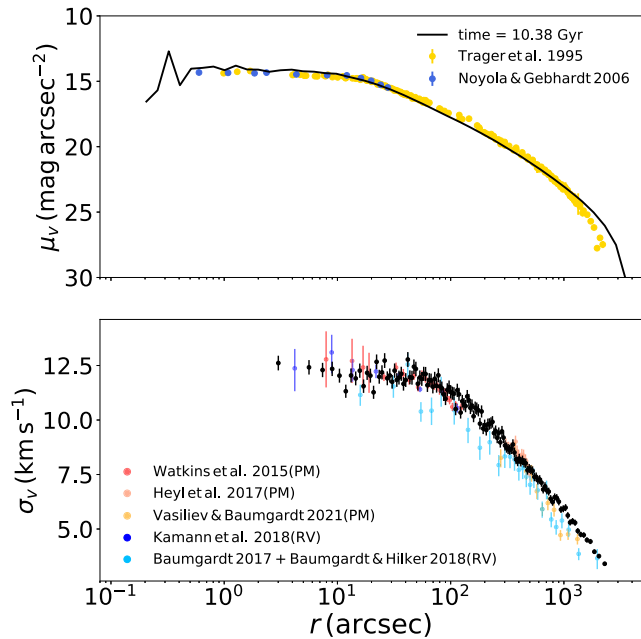
Figure 13. A massive model at $t = 10.38$ Gyr with initial binary fraction $f_b = 8\%$ (the black curve and black markers). It has initial $N = 2.95e6$ and initial $r_v = 3.5$ pc. See the text for more details.

5.3. Implications for Black Hole Merger Rate

The top-light IMF is likely to reduce the total number of binary BH mergers (e.g., Weatherford et al. 2021). Over a Hubble time, the 47 Tuc simulation produces 220 binary BH mergers, including both those that merged in the cluster and those that merged after being ejected. To check how this steep power-law slope for massive stars affects binary BH mergers, we also calculate the number of mergers in the simulation with high-mass power-law slope $\alpha_2 = 2.3$ (also see Figure 12). Surprisingly, this simulation produces $\sim$2700 BHs at late times, about 15 times more than in the best-fitting 47 Tuc models, but only 210 merging binary BHs over a Hubble time. This occurs because, although it produces more BHs, the model with $\alpha_2 = 2.3$ is much less dense in the core than what we see in the best-fitting 47 Tuc simulation (Figure 12). Thus its BHs undergo fewer dynamical encounters, and there are fewer mergers per BH (e.g., Kremer et al. 2020, Figure 13). Hypothetically, however, if we were to generate 47 Tuc models with a standard Kroupa IMF, but with smaller initial virial radius and a high central density at present, more binary BH mergers should be produced (Weatherford et al. 2021). In Weatherford et al. (2021), models with a high-mass power-law slope $\alpha = 2.3$ produce more binary BH mergers than those with $\alpha = 3$. The difference may be attributed to the very different IMF, initial virial radius, and/or initial density profile used in this study than in Weatherford et al. (2021).

5.4. Binary Fraction

Binary stars play an important role in the dynamical evolution of GCs (e.g., Heggie & Hut 2003). For example, BH binaries can act as energy sources in a cluster core, delaying the core collapse of clusters (e.g., Kremer et al. 2019). Learning the primordial binary fractions of GCs can also help reveal details of the formation of GCs and the properties of their pre-GC molecular clouds. Furthermore, since the majority of stars in the Milky Way are expected to be born in clusters,

the binary fractions in GCs are also connected to that in the field (Lada & Lada 2003). However, the GC binary fractions, especially the relation between primordial and present-day binary fractions, are not well constrained (e.g., Fregeau et al. 2009; Milone et al. 2012, and references therein).

Milone et al. (2012) found the total fraction of binaries in 47 Tuc to be $\sim$2%, and the binary fractions at mass ratio $q > 0.5$, 0.6, 0.7 to be 0.009 ± 0.003, 0.007 ± 0.003, 0.005 ± 0.003, respectively, at the radial region between the cluster's observed core and half-light radii (Harris 1996, 2010 edition). Ji & Bregman (2015) obtained a binary fraction in 47 Tuc to be $3.01 \pm 0.13\%$ within about the half-light radius, using their direct counting method for binaries with high mass ratios $q > 0.5$. More recently, Mann et al. (2019) found the binary fractions in 47 Tuc for q in the ranges of 0.5–0.7, 0.7–0.9, and >0.9 to be 0.0265, 0.0098 and 0.0039, respectively. These observations are all consistent with low binary fractions.

We "observed" the binary fractions in the best-fit model by identifying binary stars in its CMD using the technique in Rui et al. (2021), which mimics the observational cuts in Milone et al. (2012). We found that at radii between the observed core and half-light radii (Harris 1996, 2010 edition), the best-fit model has binary fractions 0.0107 ± 0.00023, 0.0085 ± 0.00021, and 0.0063 ± 0.00018 at mass ratios $q > 0.5$, 0.6, and 0.7, respectively. This is consistent with the observation in Milone et al. (2012) at all three mass ratios.

To explore how changing the primordial binary fraction affects the model, we also experimented with a cluster with initial binary fraction $f_b = 8\%$, initial number of stars $N = 2.95e6$ and initial virial radius $r_v = 3.5$ pc. The small variation in the initial N and r_v is to compensate for the increased number of binaries so that the cluster has a similar initial mass to the best-fit 47 Tuc model and that its SBP and VDP at late times will fit the observations. Figure 13 compares the SBP and VDP of this model to the observations, and shows the model properties match the observations well. However, the model has binary fractions 0.0352 ± 0.00043, 0.0274 ± 0.00038, and 0.0199 ± 0.0032 at $q > 0.5$, 0.6, and 0.7, respectively, which are about three times higher than those observed in Milone et al. (2012). Furthermore, models with an 8% binary fraction may be overproducing MSPs and CVs (there are 132 MSPs and 787 CVs at 10.38 Gyr). Therefore, 47 Tuc is more likely to have a low primordial binary fraction of <8% and closer to $\sim$2%.

5.5. Rotation in 47 Tuc

Many studies have shown that 47 Tuc is rotating and has velocity anisotropy using observations from HST, Gaia, and MUSE (e.g., Watkins et al. 2015; Bellini et al. 2017; Kamann et al. 2018; Vasiliev & Baumgardt 2021). These additional dimensions of the cluster's dynamical structure can improve our understanding of how the cluster forms and evolves, and may alter the cluster properties derived from the traditional fitting of SBPs with spherically symmetric profiles such as the King profile (King 1966) or the Elson profile (Elson et al. 1987). However, CMC assumes spherical symmetry (Rodriguez et al. 2022) and is not able to treat rotation. Our model cluster's velocity dispersion is also in general isotropic[9] (see Figure 2).

---

[9] CMC can model clusters with anisotropic velocities (Rodriguez et al. 2022), but we do not consider anisotropy in this study.

Compared to the structural parameters derived in Bellini et al. (2017) from their best-fit model that took into account rotation and asymmetry, our model has a larger mass but smaller observational core and half-light radii, which are more consistent with the radii in Harris (1996, 2010 edition). Although, note that their model SBP (Bellini et al. 2017, Figure 9) is slightly lower in the core compared to Trager et al. (1995), which may contribute to the differences. Given that our best-fit model matches the observations using a spherically symmetric Elson profile, the differences in the properties of 47 Tuc when taking into account rotation and velocity anisotropy are likely small.

6. Conclusions

In this study, we simulate 47 Tuc using the Monte Carlo N-body code CMC. As one of the most massive, densest, and closest GCs in the Milky Way, there is a large data set of different 47 Tuc observations, but few N-body simulations because simulations with the cluster's mass and density are computationally time consuming. We produce 47 Tuc models that can simultaneously match the observed surface brightness, velocity dispersion, and number density profiles, the pulsar acceleration profile, and the pulsar distribution in the cluster. These models are self-consistent and take into account all of the relevant physics (e.g., BH dynamics) for the first time. The best-fit model has an IMF that is both bottom-heavy and top-light with power-law slopes $\alpha_1 = 0.4$ and $\alpha_2 = 2.8$ (Table 1). The models were also overfilling the tidal radius initially.

We report the number of exotic objects in the models that most closely match the observations; the best-fit models result in 54 MSPs, 14 LMXBs, 334 CVs, 186 BHs, 1368 NSs, and 101 BSSs in the cluster at the present day. The numbers of MSPs, LMXBs, and CVs are likely upper limits given that our simple treatments of tidal capture and giant star collision maximize binary formation, and that we do not consider duty cycles and luminosities of LMXBs and CVs. We also demonstrate that tidal capture in GCs may be important to the formation of redback MSPs and many MSPs may be formed from giant star collisions. Furthermore, an intermediate-mass black hole is not necessary to explain the pulsar accelerations observed in the cluster.

We also discuss how different density distribution profiles (King versus Elson profiles), IMFs, and binary fractions affect the observed properties of 47 Tuc, such as the binary BH merger rates. We point out that there may be a degeneracy in 47 Tuc models given a top-light IMF or an initial small virial radius, which have similar effects on reducing the number of BHs and thus the properties of the cluster. Due to the significant computational time taken to run a 47 Tuc-size simulation, we did not explore systematically the vast parameter space of initial conditions for star clusters, or the full range of uncertainties in our various assumptions and input parameters (e.g., characterizing the BH and NS natal kicks, or the treatment of binary mass transfer and common-envelope phases). Therefore, we do not claim that our best-fit model presented here is unique.

Appendix A
Single–single Interactions in CMC

Figure 14 demonstrates the treatment of all single–single interactions including tidal captures and giant star collisions in CMC.
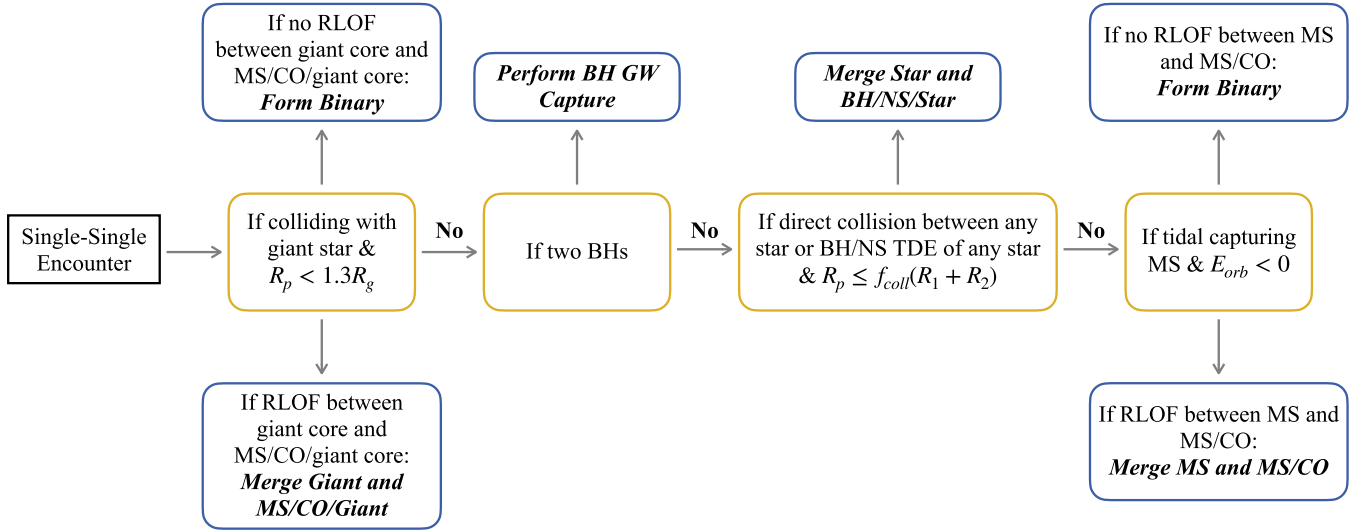
Figure 14. Flowchart illustrating single–single dynamical encounters in CMC. Note that if both stars are giants, the collision is performed when $r_p < 1.3(R_{g1} + R_{g2})$. Default $f_{\rm coll} = 1$ in CMC. "MS" is main-sequence stars, "CO" is compact objects, "RLOF" is Roche lobe overflow, and "TDE" is tidal disruption events.

Appendix B
Comparison with Detailed Stellar Models

To verify that our simple application of polytropic stellar models agrees with more sophisticated calculations, we compare the oscillation energy and the critical capture pericenter distance between the tidal capture of two MS stars in this study with those in McMillan et al. (1987). Figure 15 shows the comparison. For $\eta \lesssim 10$, the oscillation energy calculated with polytropic stellar models agrees well with the more detailed stellar models. At $v_\infty \sim 10\,{\rm km\,s^{-1}}$ (the velocity dispersion of typical GCs and of 47 Tuc), there can be as big as a $\sim 20\%$ discrepancy in the critical pericenter distances between different stellar models for low-mass MS stars, which is not likely to affect the outcomes of tidal capture (see Section 5 and Appendix C). For simplicity, we assume that the structure of the stars does not change during tidal capture.
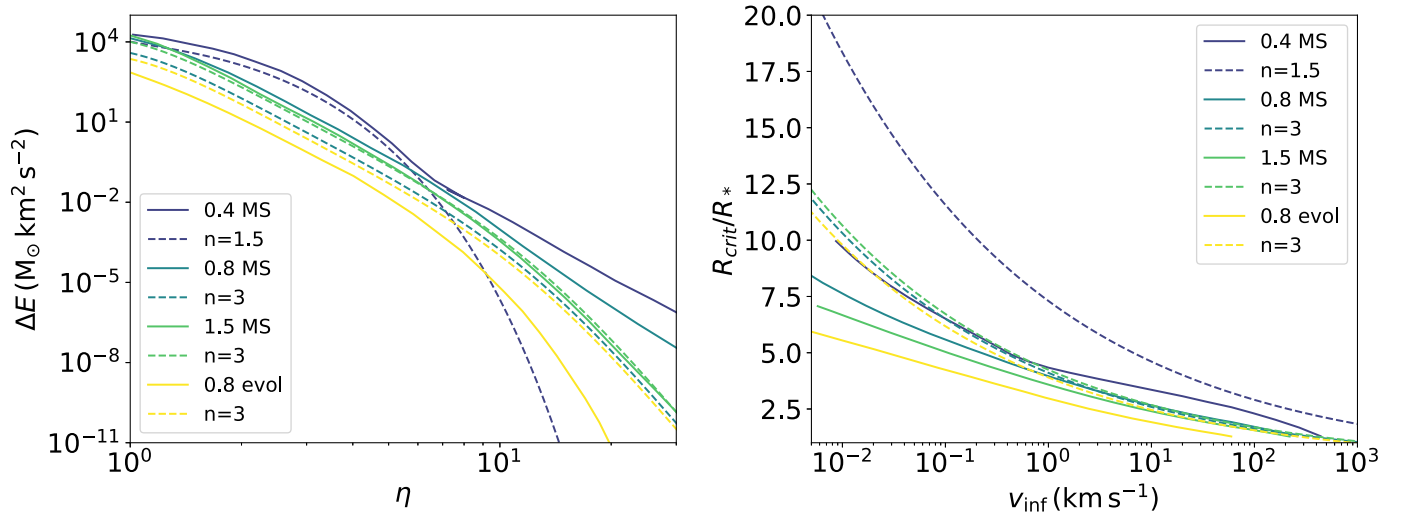
Figure 15. Comparison between polytropic stellar models to detailed stellar models of McMillan et al. (1987). The left panel shows the tidal energy dissipation in terms of the dimensionless transit time. The right panel shows the ratio of the critical capture periastron separation to the radius of the star as a function of the relative velocity at infinity. "MS" is for MS stars, and "evol" is for stars just evolving off the main sequence.

Appendix C
Tidal Capture and Giant Star Collision Uncertainties

We are only considering tidal capture and giant star collision during single–single encounters in this study for simplicity. To estimate how the tidal capture and giant star collision rates will be affected if we include these interactions during binary–single and binary–binary encounters, we calculated the direct collision ("sticky-sphere" collision) rates for all types of stars in the CMC Cluster Catalog models (Kremer et al. 2020). We found that for MS stars and compact objects, direct collisions occur ∼2.5 times more frequently during binary–single and binary–binary encounters than single–single encounters. However, for giant stars, direct collisions are ∼5 times more frequent in single–single encounters. Thus, including giant star collisions in binary interactions is not likely to have a large influence on the overall rates, but the tidal capture rates are likely to at least double if the interaction is occurring in binary–binary and binary–single encounters. The implementation of tidal capture into Fewbody is currently undergoing (M. Vick et al. 2022, in preparation).

We assume, during common-envelope evolution, $\alpha = 1$ (parameter for scaling the efficiency of transferring orbital energy to the envelope) and $\lambda = 0.5$ (binding energy factor for the stellar envelope) in binary evolution in COSMIC (Hurley et al. 2002; Breivik et al. 2020). These simple values give us a sense of how giant star collisions vary with different values for α and λ. For example, for a smaller binding energy factor where λ is close to zero, the release of recombination energy that can enhance envelope ejection is turned off (Claeys et al. 2014) and all giant star collisions lead to mergers. We point out that the values of α and λ are highly uncertain (e.g., Ivanova et al. 2013, and references therein). Previous studies suggested an α from as small as ∼0.2 (Zorotovic et al. 2010; Toonen & Nelemans 2013; Camacho et al. 2014) to as large as ∼5 (Fragos et al. 2019). In addition, while most treatments adopt a constant λ, it is more likely that λ varies according to the types of stars and the stellar mass fraction in their envelopes

(Ivanova 2011). By varying α and λ and matching the number and properties of compact objects in GCs, especially pulsars, we could put better constraints on these two parameters, but this is beyond the scale of this study.

Previous studies have shown that tidal-force induced oscillation during tidal capture may cause large fluctuation and instability in MS stars, and may lead to their disruption (e.g., Kochanek 1992). We compare the binding energy of the MS stars $0.15 \frac{GM^2}{R}$ with their induced oscillation energy during tidal capture (Kochanek 1992). Only four stars are disrupted for all R_p, and none are disrupted when only considering $\frac{R_p}{R} < 1.3 \left(\frac{M_T}{2M} \right)^{\frac{1}{3}}$ (Kochanek 1992), where M and R are the mass and radius of the MS stars, respectively, and M_T is the total mass of the two interacting objects.

Figure 15 shows some discrepancies in the oscillation energy and critical radius calculated with polytropic stellar models and detailed stellar models (McMillan et al. 1987). For the oscillation energy induced by tidal force (left panel), the most pronounced difference is for $n = 1.5$ and 0.4 MS when $\eta \gtrsim 6$. In our 47 Tuc simulation, only about 4% of tidal capture encounters have $\eta > 6$, so the difference for $\eta > 6$ has a negligible effect on the final tidally captured binaries. For the critical radius (right panel), the largest deviation is ∼20% again for $n = 1.5$ and 0.4 MS at $v_{inf} \sim 10$ km s^{-1}. However, these parameters mostly involve interactions between low-mass MS stars and other low-mass MS stars or WDs. The discrepancy will not affect the number of tidally captured NS–MS star binaries.

Appendix D
All 47 Tuc-size Simulations

Table 3 shows all simulations run to explore the specific initial parameter space for 47 Tuc. Table 4 shows the mean and standard deviation values of the present-day properties for best- and near-fit models from simulations 1–3 in Table 3.

Table 3
Initial Conditions of All Simulations

| No.	N_{init} 10^6	R_ν pc	γ/W_0	R_{max} R_ν	Z	R_{tidal} pc	f_b	Profile	M_{min} $M_\odot$	α_1	M_{br1} $M_\odot$	α_2	M_{br2} $M_\odot$	α_3	M_{max} $M_\odot$	M_{init} $10^6 M_\odot$
1[*]	3.00	4.0	2.1	200	0.0038	182.17	0.022	E	0.08	0.4	0.8	2.8	⋯	⋯	150	2.48
2	3.00	4.0	2.1	200	0.0038	149	0.022	E	0.08	0.4	0.8	2.8	⋯	⋯	150	2.52
3	2.95	3.5	2.1	200	0.0038	171	0.08	E	0.08	0.4	0.8	2.8	⋯	⋯	150	2.51
4	0.80	4.0	2.1	200	0.0038	182.17	0.022	E	0.08	0.4	0.8	1.8	⋯	⋯	150	2.57
5	1.23	4.0	2.1	200	0.0038	182.17	0.022	E	0.08	0.4	0.8	2	⋯	⋯	150	2.58
6	1.96	4.0	2.1	200	0.0038	182.17	0.022	E	0.08	0.4	0.8	2.3	⋯	⋯	150	2.56
7	2.80	4.0	2.1	200	0.004	171	0.022	E	0.08	0.52	0.5	1.35	1	2.49	150	2.66
8	2.80	3.0	2.1	200	0.004	171	0.022	E	0.08	0.52	0.5	1.35	1	2.49	150	2.66
9	2.00	1.4	7.5	⋯	0.0038	159.15	0.022	K	0.08	0.4	0.8	2.8	⋯	⋯	150	1.66
10	2.00	1.8	7.5	⋯	0.0038	159.15	0.022	K	0.08	0.4	0.8	2.8	⋯	⋯	150	1.66
11	2.00	1.8	2.1	300	0.0038	159.15	0.022	E	0.08	0.4	0.8	2.8	⋯	⋯	150	1.66
12	2.00	4	2.1	300	0.0038	159.15	0.022	E	0.08	0.4	0.8	2.8	⋯	⋯	150	1.66
13	2.40	4	2.1	300	0.0038	169.13	0.022	E	0.08	0.4	0.8	2.8	⋯	⋯	150	1.99
14	2.00	1.84	7.5	⋯	0.0038	158.32	0.022	K	0.08	0.4	0.8	2.8	⋯	⋯	50	1.63
15	2.00	1.84	7.5	⋯	0.0038	129.43	0.022	K	0.08	0.4	0.8	2.8	⋯	⋯	50	1.63
16	3.00	4.0	2.1	75	0.0038	182.16	0.022	E	0.08	0.4	0.8	2.8	⋯	⋯	150	2.48

Note. Columns from left to right: number of objects, virial radius, power-law slope of an Elson profile or King concentration parameter, maximum radius (in virial radius) to sample the cluster, metallicity, tidal radius, binary fraction, E–Elson or K–King profile, masses and slopes of the IMF, and total cluster mass. [*]–the best-fit 47 Tuc simulation. Nos. 2 and 3 also fit the SBPs and VDPs, so are used for calculating the more general uncertainties of the properties and numbers shown in Table 2. Nos. 4 and 5 are disrupted at early times of the simulation. The run of No. 8 was stopped at early times because it is very computationally expensive. The IMF for Nos. 7 and 8 is adopted from Hénault-Brunet et al. (2019). The tidal radius 171 pc is adopted from Lane et al. (2012).

Table 4
Present-day Properties of Best- and Near-fit Models

	$Mass$ $M_\odot$	r_c pc	r_h pc	r_{cobs} arcmin	r_{hlobs} arcmin	N_{BH}	N_{BH-BH}	N_{NS}	N_{LMXB}	N_{MSP}	$N_{young\ psr}$	N_{CV}	N_{BSS}	$N_{tcNS-MS}$
μ	9.86×10^5	0.82	6.48	0.33	2.64	160	2	1369	17	50	0	412	135	5
σ	2.82×10^4	0.09	0.34	0.04	0.22	32	1	1	4	3	0	177	72	3

Note. Similar to Table 2, mean values and standard deviations of cluster properties and numbers of compact objects. The last column shows the average number of tidally captured NS–MS binaries and its standard deviation. We relaxed the χ^2 selection criterion described in Section 3 to include more snapshots at ∼8.3−13.5 Gyr from the best-fit 47 Tuc simulation, and also snapshots from simulation Nos. 2 (∼9−13.1 Gyr) and 3 (∼10−13.6 Gyr) in Table 3. Most mean values and standard deviations stay similar to those in Table 2. There are large standard deviations for the numbers of CVs and BSSs, because simulation No. 3, with a higher initial binary fraction, produces many more of these systems.

ORCID iDs

Claire S. Ye ⓘ https://orcid.org/0000-0001-9582-881X
Kyle Kremer ⓘ https://orcid.org/0000-0002-4086-3180
Carl L. Rodriguez ⓘ https://orcid.org/0000-0003-4175-8881
Nicholas Z. Rui ⓘ https://orcid.org/0000-0002-1884-3992
Newlin C. Weatherford ⓘ https://orcid.org/0000-0002-9660-9085
Sourav Chatterjee ⓘ https://orcid.org/0000-0002-3680-2684
Giacomo Fragione ⓘ https://orcid.org/0000-0002-7330-027X
Frederic A. Rasio ⓘ https://orcid.org/0000-0002-7132-418X

References

Abbott, R., Abbott, T. D., Abraham, S., et al. 2021, ApJL, 913, L7
Abdo, A. A., Ackermann, M., Ajello, M., et al. 2009, Sci, 325, 845
Amaro-Seoane, P., & Chen, X. 2016, MNRAS, 458, 3075
Antognini, J. M., Shappee, B. J., Thompson, T. A., & Amaro-Seoane, P. 2014, MNRAS, 439, 1079
Bahramian, A., Heinke, C. O., Tudor, V., et al. 2017, MNRAS, 467, 2199
Baumgardt, H. 2017, MNRAS, 464, 2174
Baumgardt, H., & Hilker, M. 2018, MNRAS, 478, 1520
Baumgardt, H., Hilker, M., Sollima, A., & Bellini, A. 2019, MNRAS, 482, 5138
Baumgardt, H., Sollima, A., Hilker, M., Bellini, A., & Vasiliev, E. 2021, https://people.smp.uq.edu.au/HolgerBaumgardt/globular/

Baumgardt, H., & Vasiliev, E. 2021, MNRAS, 505, 5957
Belczynski, K., Kalogera, V., & Bulik, T. 2002, ApJ, 572, 407
Bellini, A., Bianchini, P., Varri, A. L., et al. 2017, ApJ, 844, 167
Bhattacharya, S., Heinke, C. O., Chugunov, A. I., et al. 2017, MNRAS, 472, 3706
Bildsten, L. 2002, ApJL, 577, L27
Breivik, K., Coughlin, S., Zevin, M., et al. 2020, ApJ, 898, 71
Brogaard, K., VandenBerg, D. A., Bedin, L. R., et al. 2017, MNRAS, 468, 645
Camacho, J., Torres, S., García-Berro, E., et al. 2014, A&A, 566, A86
Casertano, S., & Hut, P. 1985, ApJ, 298, 80
Chatterjee, S., Fregeau, J. M., Umbreit, S., & Rasio, F. A. 2010, ApJ, 719, 915
Chatterjee, S., Rodriguez, C. L., & Rasio, F. A. 2017, ApJ, 834, 68
Chatterjee, S., Umbreit, S., Fregeau, J. M., & Rasio, F. A. 2013, MNRAS, 429, 2881
Chen, H.-L., Chen, X., Tauris, T. M., & Han, Z. 2013, ApJ, 775, 27
Choksi, N., Gnedin, O. Y., & Li, H. 2018, MNRAS, 480, 2343
Claeys, J. S. W., Pols, O. R., Izzard, R. G., Vink, J., & Verbunt, F. W. M. 2014, A&A, 563, A83
Clark, G. W. 1975, ApJL, 199, L143
Da Costa, G. S., & Freeman, K. C. 1985, in IAU Symp. 113, Dynamics of Star Clusters, ed. J. Goodman & P. Hut (Cambridge: Cambridge Univ. Press), 69
Davoust, E. 1986, A&A, 166, 177
de Boer, T. J. L., Gieles, M., Balbinot, E., et al. 2019, MNRAS, 485, 4906
de Marchi, G., Paresce, F., & Ferraro, F. R. 1993, ApJS, 85, 293
Deloye, C. J., & Bildsten, L. 2003, ApJ, 598, 1217
Dotter, A., Sarajedini, A., Anderson, J., et al. 2010, ApJ, 708, 698
Duquennoy, A., & Mayor, M. 1991, A&A, 500, 337
Edmonds, P. D., Gilliland, R. L., Guhathakurta, P., et al. 1996, ApJ, 468, 241

Edmonds, P. D., Gilliland, R. L., Heinke, C. O., & Grindlay, J. E. 2003a, ApJ, 596, 1177
Edmonds, P. D., Gilliland, R. L., Heinke, C. O., & Grindlay, J. E. 2003b, ApJ, 596, 1197
Elson, R. A. W., Fall, S. M., & Freeman, K. C. 1987, ApJ, 323, 54
Elson, R. A. W., Fall, S. M., & Freeman, K. C. 1989, ApJ, 336, 734
Fabian, A. C., Pringle, J. E., & Rees, M. J. 1975, MNRAS, 172, 15
Fragos, T., Andrews, J. J., Ramirez-Ruiz, E., et al. 2019, ApJL, 883, L45
Fregeau, J. M., Cheung, P., Portegies Zwart, S., & Rasio, F. 2004, MNRAS, 352, 1
Fregeau, J. M., Gurkan, M. A., Joshi, K. J., & Rasio, F. A. 2003, ApJ, 593, 772
Fregeau, J. M., Ivanova, N., & Rasio, F. A. 2009, ApJ, 707, 1533
Fregeau, J. M., & Rasio, F. A. 2007, ApJ, 658, 1047
Freire, P. C. C., & Ridolfi, A. 2018, MNRAS, 476, 4794
Freire, P. C. C., Ridolfi, A., Kramer, M., et al. 2017, MNRAS, 471, 857
Fryer, C. L., Belczynski, K., Wiktorowicz, G., et al. 2012, ApJ, 749, 91
Gieles, M., & Zocchi, A. 2015, MNRAS, 454, 576
Giersz, M., & Heggie, D. C. 2011, MNRAS, 410, 2698
Gilliland, R. L., Edmonds, P. D., Petro, L., Saha, A., & Shara, M. M. 1995, ApJ, 447, 191
Ginzburg, S., & Quataert, E. 2020, MNRAS, 495, 3656
Guhathakurta, P., Yanny, B., Schneider, D. P., & Bahcall, J. N. 1992, AJ, 104, 1790
Haghi, H., Khalaj, P., Hasani Zonoozi, A., & Kroupa, P. 2017, ApJ, 839, 60
Hansen, B. M. S., Kalirai, J. S., Anderson, J., et al. 2013, Natur, 500, 51
Harris, W. E. 1996, AJ, 112, 1487
Harris, W. E. 2010, arXiv:1012.3224
Heggie, D., & Hut, P. 2003, The Gravitational Million-Body Problem: A Multidisciplinary Approach to Star Cluster Dynamics (Cambridge: Cambridge Univ. Press)
Heggie, D. C. 1975, MNRAS, 173, 729
Heinke, C. O., Grindlay, J. E., Edmonds, P. D., et al. 2005, ApJ, 625, 796
Heinke, C. O., Grindlay, J. E., Lugger, P. M., et al. 2003, ApJ, 598, 501
Hénault-Brunet, V., Gieles, M., Sollima, A., et al. 2019, MNRAS, 483, 1400
Hénon, M. 1971a, Ap&SS, 14, 151
Hénon, M. 1971b, Ap&SS, 13, 284
Heyl, J., Caiazzo, I., Richer, H., et al. 2017, ApJ, 850, 186
Hobbs, G., Lorimer, D. R., Lyne, A. G., & Kramer, M. 2005, MNRAS, 360, 974
Hurley, J. R., Pols, O. R., & Tout, C. A. 2000, MNRAS, 315, 543
Hurley, J. R., Tout, C. A., & Pols, O. R. 2002, MNRAS, 329, 897
Illingworth, G., & Illingworth, W. 1976, ApJS, 30, 227
Ivanova, N. 2011, in ASP Conf. Ser. 447, Evolution of Compact Binaries, ed. L. Schmidtobreick, M. R. Schreiber, & C. Tappert (San Francisco, CA: ASP), 91
Ivanova, N., Heinke, C. O., Rasio, F. A., et al. 2006, MNRAS, 372, 1043
Ivanova, N., Justham, S., Chen, X., et al. 2013, A&ARv, 21, 59
Ji, J., & Bregman, J. N. 2015, ApJ, 807, 32
Joshi, K. J., Nave, C. P., & Rasio, F. A. 2001, ApJ, 550, 691
Joshi, K. J., Rasio, F. A., & Portegies Zwart, S. 2000, ApJ, 540, 969
Kamann, S., Husser, T. O., Dreizler, S., et al. 2018, MNRAS, 473, 5591
Kaplan, D. L., Stovall, K., van Kerkwijk, M. H., Fremling, C., & Istrate, A. G. 2018, ApJ, 864, 15
Kiel, P. D., Hurley, J. R., Bailes, M., & Murray, J. R. 2008, MNRAS, 388, 393
Kim, S. S., & Lee, H. M. 1999, A&A, 347, 123
King, I. R. 1966, AJ, 71, 64
Kızıltan, B., Baumgardt, H., & Loeb, A. 2017, Natur, 542, 203
Knigge, C. 2012, MmSAI, 83, 549
Kochanek, C. S. 1992, ApJ, 385, 604
Kremer, K., Chatterjee, S., Rodriguez, C. L., & Rasio, F. A. 2018a, ApJ, 852, 29
Kremer, K., Chatterjee, S., Ye, C. S., Rodriguez, C. L., & Rasio, F. A. 2019, ApJ, 871, 38
Kremer, K., Rui, N. Z., Weatherford, N. C., et al. 2021, ApJ, 917, 28
Kremer, K., Ye, C. S., Chatterjee, S., Rodriguez, C. L., & Rasio, F. A. 2018b, ApJL, 855, L15
Kremer, K., Ye, C. S., Rui, N. Z., et al. 2020, ApJS, 247, 48
Kroupa, P. 2001, MNRAS, 322, 231
Lada, C. J., & Lada, E. A. 2003, ARA&A, 41, 57
Lane, R. R., Küpper, A. H. W., & Heggie, D. C. 2012, MNRAS, 423, 2845
Lee, H. M., & Ostriker, J. P. 1986, ApJ, 310, 176
Leiner, E. M., & Geller, A. 2021, ApJ, 908, 229
Lombardi, J. C. J., Proulx, Z. F., Dooley, K. L., et al. 2006, ApJ, 640, 441
Lorimer, D. R. 2008, LRR, 11, 8
Mackey, A. D., & Gilmore, G. F. 2003, MNRAS, 338, 85
Mann, C. R., Richer, H., Heyl, J., et al. 2019, ApJ, 875, 1

Marks, M., Kroupa, P., Dabringhausen, J., & Pawlowski, M. S. 2012, MNRAS, 422, 2246
McLaughlin, D. E., Anderson, J., Meylan, G., et al. 2006, ApJS, 166, 249
McLaughlin, D. E., & van der Marel, R. P. 2005, ApJS, 161, 304
McMillan, S. L. W., McDermott, P. N., & Taam, R. E. 1987, ApJ, 318, 261
Meylan, G. 1988, A&A, 191, 215
Meylan, G. 1989, A&A, 214, 106
Miller-Jones, J. C. A., Strader, J., Heinke, C. O., et al. 2015, MNRAS, 453, 3918
Milone, A. P., Piotto, G., Bedin, L. R., et al. 2012, A&A, 540, A16
Miocchi, P., Lanzoni, B., Ferraro, F. R., et al. 2013, ApJ, 774, 151
Morscher, M., Pattabiraman, B., Rodriguez, C., Rasio, F. A., & Umbreit, S. 2015, ApJ, 800, 9
Noyola, E., & Gebhardt, K. 2006, AJ, 132, 447
Parada, J., Richer, H., Heyl, J., Kalirai, J., & Goldsbury, R. 2016, ApJ, 830, 139
Pattabiraman, B., Umbreit, S., Liao, W.-K., et al. 2013, ApJ, 204, 15
Paulo Freire's pulsar catalog 2021, http://www.naic.edu/~pfreire/GCpsr.html
Pfahl, E., Rappaport, S., & Podsiadlowski, P. 2002, ApJ, 573, 283
Phinney, E. S. 1992, RSPTA, 341, 39
Plummer, H. C. 1911, MNRAS, 71, 460
Podsiadlowski, P., Langer, N., Poelarends, A. J. T., et al. 2004, ApJ, 612, 1044
Portegies Zwart, S. F., McMillan, S. L. W., & Gieles, M. 2010, ARA&A, 48, 431
Portegies Zwart, S. F., & Meinen, A. T. 1993, A&A, 280, 174
Press, W. H., & Teukolsky, S. A. 1977, ApJ, 213, 183
Pryor, C., & Meylan, G. 1993, in ASP Conf. Ser. 50, Structure and Dynamics of Globular Clusters, ed. S. G. Djorgovski & G. Meylan (San Francisco, CA: ASP), 357
Ransom, S. M. 2008, in IAU Symp. 246, Dynamical Evolution of Dense Stellar, ed. E. Vesperini, M. Giersz, & A. Sills (Cambridge: Cambridge Univ. Press), 291
Ray, A., Kembhavi, A. K., & Antia, H. M. 1987, A&A, 184, 164
Ridolfi, A., Freire, P. C. C., Torne, P., et al. 2016, MNRAS, 462, 2918
Ridolfi, A., Gautam, T., Freire, P. C. C., et al. 2021, MNRAS, 504, 1407
Rivera Sandoval, L. E., van den Berg, M., Heinke, C. O., et al. 2018, MNRAS, 475, 4841
Roberts, M. S. E. 2013, in IAU Symp. 291, Neutron Stars and Pulsars: Challenges and Opportunities after 80 years, ed. J. van Leeuwen (Cambridge: Cambridge Univ. Press), 127
Rodriguez, C. L., Amaro-Seoane, P., Chatterjee, S., et al. 2018b, PhRvD, 98, 123005
Rodriguez, C. L., Amaro-Seoane, P., Chatterjee, S., & Rasio, F. A. 2018a, PhRvL, 120, 151101
Rodriguez, C. L., Kremer, K., Chatterjee, S., et al. 2021, RNAAS, 5, 19
Rodriguez, C. L., Morscher, M., Wang, L., et al. 2016, MNRAS, 463, 2109
Rodriguez, C. L., Weatherford, N. C., Coughlin, S. C., et al. 2022, ApJS, 258, 22
Rui, N. Z., Kremer, K., Weatherford, N. C., et al. 2021, ApJ, 912, 102
Santiago, B. X., Elson, R. A. W., & Gilmore, G. F. 1996, MNRAS, 281, 1363
Shara, M. M., Bergeron, L. E., Gilliland, R. L., Saha, A., & Petro, L. 1996, ApJ, 471, 804
Spitzer, L. 1987, Dynamical Evolution of Globular Clusters (Princeton, NJ: Princeton Univ. Press)
Strader, J., Swihart, S., Chomiuk, L., et al. 2019, ApJ, 872, 42
Thompson, I. B., Kaluzny, J., Rucinski, S. M., et al. 2010, AJ, 139, 329
Thompson, I. B., Udalski, A., Dotter, A., et al. 2020, MNRAS, 492, 4254
Toonen, S., & Nelemans, G. 2013, A&A, 557, A87
Trager, S. C., King, I. R., & Djorgovski, S. 1995, AJ, 109, 218
Umbreit, S., Fregeau, J. M., Chatterjee, S., & Rasio, F. A. 2012, ApJ, 750, 31
VandenBerg, D. A., Brogaard, K., Leaman, R., & Casagrande, L. 2013, ApJ, 775, 134
Vasiliev, E., & Baumgardt, H. 2021, MNRAS, 505, 5978
Wang, L., Spurzem, R., Aarseth, S., et al. 2015, MNRAS, 450, 4070
Watkins, L. L., van der Marel, R. P., Bellini, A., & Anderson, J. 2015, ApJ, 803, 29
Weatherford, N. C., Chatterjee, S., Kremer, K., & Rasio, F. A. 2020, ApJ, 898, 162
Weatherford, N. C., Chatterjee, S., Rodriguez, C. L., & Rasio, F. A. 2018, ApJ, 864, 13
Weatherford, N. C., Fragione, G., Kremer, K., et al. 2021, ApJL, 907, L25
Wilson, C. P. 1975, AJ, 80, 175
Ye, C. S., Kremer, K., Chatterjee, S., Rodriguez, C. L., & Rasio, F. A. 2019, ApJ, 877, 122
Zorotovic, M., Schreiber, M. R., Gänsicke, B. T., & Nebot Gómez-Morán, A. 2010, A&A, 520, A86